Numerical study of turbulent coherent structures and bubble entrainment under surfzone breaking waves

GANGFENG MA[1]†, JAMES T. KIRBY[1] AND FENGYAN SHI[1]

[1] Center for Applied Coastal Research, University of Delaware, Newark, DE 19716, USA

(Received ?? and in revised form ??)

Wave breaking in the surf zone entrains large volumes of bubbles into the water column, producing a complex two-phase bubbly flow field. The interactions among dispersed bubbles, mean flow and turbulence are still poorly understood. In this study, we perform a large-eddy simulation of polydisperse bubbly flow under a surfzone spilling breaking wave to investigate the turbulent coherent structures and their interactions with dispersed bubbles. The numerical model we employ explicitly accounts for bubble effects on momentum and turbulence in the liquid phase as well as turbulent transport on bubbles. The model is shown to predict surface elevation evolution and wave height distribution fairly well in a laboratory-scale surf zone, and is capable of capturing obliquely descending eddies and downbursts of turbulent fluid. Our study has revealed that the turbulent coherent structures play an important role in turbulent kinetic energy and momentum transport as well as bubble entrainment. These coherent structures tend to transport bubbles offshore and more deeply into the water column. The mechanisms of the generation of streamwise vortices are discussed. The presence of bubbles may suppress turbulence and enstrophy, and subsequently attenuate vortex evolution processes.

1. Introduction

Wave breaking in the surf zone entrains large volumes of bubbles into the water column. These bubbles are involved in intense interactions with mean flow and turbulence, producing a complex two-phase bubbly flow field. It is well known that the presence of bubbles can suppress liquid phase turbulence (Wang et al., 1987; Kataoka and Serizawa, 1989; Serizawa and Kataoka, 1990; Lopez de Bertodano et al., 1994). Other studies have also revealed that bubbles may alter the local vorticity field and consequently deform or displace the vortex structure (Sridhar and Katz, 1999; Watanabe et al., 2005). Therefore, in order to study the turbulent bubbly flow under breaking waves, it is necessary to describe the dynamics of breaking waves as two-phase (gas-liquid) flow with air bubbles of appropriate size distribution.

Several studies based on laboratory experiments have revealed that turbulent bubbly flow in surf-zone breaking waves is characterized by large-scale, organized flow structures which occur intermittently in space and time. Nadaoka et al. (1989) studied regular breaking waves on a plane beach and found that wave breaking generates spanwise vortices with axes parallel to the crest line around the wave crest. The flow structure quickly

† Email address for correspondence: gma@udel.edu

becomes three-dimensional behind the wave crest, evolving into obliquely descending eddies. Kubo and Sunamura (2001) found another type of coherent structure, called a downburst, in their laboratory study of a spilling breaking wave. The downbursts show no significant vortical motion, but can carry a large amount of turbulent kinetic energy (TKE) into the water column. Ting (2006, 2008) systematically studied the forms and evolution of coherent structures. It was found that large-scale turbulence in the middle of the water column first arrived in the form of a downburst of turbulent fluid, which was accompanied by two counter-rotating vortices. The turbulent kinetic energy and turbulence stresses showed episodic turbulent events near the free surface but more sporadic turbulence in the lower layer.

In addition to the above-mentioned studies, there are also other important laboratory investigations on the nature of breaking wave induced turbulence. For example, Ting and Kirby (1994, 1995, 1996) conducted comprehensive studies on the turbulence transport under different types of surf zone breaking waves, and found significant differences in the characteristics of turbulence transport in spilling and plunging breakers. Under plunging breakers, the turbulent kinetic energy is transported landward and dissipated within one wave cycle. In spilling breaking waves, turbulent kinetic energy is transported seaward and the dissipation rate is much slower. Chang and Liu (1998, 1999) applied PIV to investigate turbulence generated by breaking wave in water of intermediate depth. A TKE budget was analyzed to show that turbulence production and dissipation under the trough level were of the same order of magnitude, but not identical. Turbulence advection, production, and dissipation were equally important, while turbulence diffusion was almost negligible. Cox and Kobayashi (2000) used LDV measurements to show the existence of intense, intermittent turbulence in the surf zone for spilling breaking waves. The intermittent turbulent events could extend into the bottom boundary layer, and account for a significant fraction of turbulent kinetic energy and shear stress at the boundary. Sou et al. (2010) used PIV to study evolution of turbulent structures in the surf and swash zone. They found that large-scale turbulent structures are closely associated with breaking wave and bore-generated turbulence in the surf zone. The large-scale turbulence energy cascades to smaller scales from the outer surf zone to the swash zone. Smaller-scale energy injection during the latter stage of downwash phase is associated with bed-generated turbulence. The TKE decay resembles the decay of grid turbulence during the latter stage of uprush and the early stage of downwash.

Besides laboratory experiments, a powerful tool to investigate the turbulent flow field in the surf zone and swash zone is solving the Navier-Stokes equations numerically with assistance of turbulence closure models. Early attempts to study turbulent flow in the surf zone numerically were based on 2-D RANS simulation coupled with a surface-capturing model, such as Volume-of-Fluid (VOF) model. For example, Lin and Liu (1998a,b) conducted 2-D RANS simulations to investigate the turbulence transport and vorticity dynamics under spilling and plunging breaking waves. They showed that the model could predict surface elevation and velocity well, but the predicted turbulence in the inner surf zone is generally 25% to 50% higher than experimental measurements (Ting and Kirby, 1995, 1996). They attribute this overestimation of turbulence to the k-ϵ turbulence closure model, which cannot accurately predict the initiation of turbulence in a rapidly distorted shear flow region such as in the initial stage of wave breaking (Shao and Ji, 2006). However, Ma et al. (2011) found that the overestimation of turbulence by a 2-D RANS simulation is also induced by the neglect of dispersed bubble effects. Watanabe and Saeki (1999) investigated the vorticity evolution and the emergence of the spanwise velocity component during wave breaking using three-dimensional large eddy simulation (LES), with a sub-grid scale viscosity model based on the renormalization group theory.

This work was extended by Watanabe et al. (2005) to investigate the vorticity and strain field for both plunging and spilling breakers. Their study reveals the possible generation mechanism of obliquely descending eddies during wave breaking. They argued that the obliquely descending eddies are essentially counter-rotating streamwise vortices, which are vortex loops produced by stretching and bending of perturbed vorticity in the saddle region between the rebounding jet and the primary spanwise vortex. Christensen and Deigaard (2001) developed a model for simulating wave breaking, large-scale water motions and turbulence. Their model consists of a free surface model using the surface marker method combined with a three-dimensional model that solves the flow equations. They successfully reproduced obliquely descending eddies under different types of breakers. They also revealed that the turbulence in spilling breakers is generated in a series of eddies in the shear layer under the surface roller, while in strong plunging breakers, turbulence originates to a large degree from the topologically generated vorticity. The turbulence generated at the plunging point is almost immediately distributed over the entire water depth by large organized vortices. Christensen (2006) conducted another LES simulation based on VOF method to study wave setup, undertow and turbulence in breaking waves. He found that results for wave height decay and undertow are satisfactory with a rather coarse resolution, but the turbulence levels tend to be over-predicted. Lubin et al. (2006) carried out a three-dimensional large eddy simulation of plunging breaking waves by solving the Navier-Stokes equations both in air and water. They discussed the physical processes of overturning, splash-up, vortex generation, air entrainment and energy dissipation. Lakehal and Liovic (2006, 2011) carried out large eddy simulations to investigate wave breaking on a steep beach. The free surface in their model was tracked by the VOF method featuring piecewise planar interface reconstructions on a twice-as-fine mesh. The Smagorinsky sub-grid scale model is coupled with a new scheme for turbulence decay treatment on the air-side of highly deformable free surfaces. They analyzed the energy transfer between the mean flow and the wave modes, and studied wave-turbulence interaction. They found that wave breaking is accompanied by intermittent generation of local vortices and increased surface wrinkling. The turbulent kinetic energy budget and the energy decay are linked to the localized incidence of coherent structures in the liquid. The energy spectra exhibit an undulation between two-dimensional turbulence -3 slope and fully developed three-dimensional -5/3 slope depending on the position.

Although efforts have been carried out to understand air entrainment under plunging breaking waves (Lubin et al., 2006; Lakehal and Liovic, 2011), there still remain issues about turbulent bubbly flow in the surf zone that have not been well resolved. For example, the effects of large-scale coherent structures on turbulent transport and bubble entrainment under breaking waves need further investigation. Interactions between dispersed bubbles (bubbles that cannot be directly resolved by VOF approach) and large-scale turbulent coherent structures are not well understood yet. Bubble transport and evolution of bubble size spectrum by longshore and rip currents in the surf zone have to be studied as well. In this paper, we attempt to address some of these issues. Because the length scale involved in bubble entrainment is too small to be directly resolved by the VOF approach, it is necessary to employ a polydisperse two-fluid model to describe bubble transport under breaking waves. We have developed a polydisperse two-fluid (gas-liquid) model (Carrica et al., 1999; Ma et al., 2011), which has been successfully implemented in an existing 3D VOF code TRUCHAS (Wu et al., 2004; Liu et al., 2005; Ma et al., 2011). The model is employed to perform a comprehensive analysis of the turbulent bubbly flow in surf-zone breaking waves. Air bubble effects are directly accounted for in the numerical simulation. In order to study the interactions between air bubbles and large-scale turbulence, we first analyze the instantaneous turbulent co-

herent structures under breaking waves and their effects on momentum and turbulence transport. Then, interactions between air bubbles and turbulent coherent structures are investigated. Bubble effects on turbulence and vorticity fields are discussed.

The paper is organized as follows. In section 2, the numerical formulations including governing equations, turbulence closure and boundary conditions are briefly introduced. In section 3, the numerical results about turbulent vortex structures and downbursts of turbulent fluid are presented. The evolution of vortex structures and their effects on turbulent transport, Reynolds stress distribution as well as bubble entrainment are investigated. Section 4 discusses the interactions between turbulent coherent structures and dispersed bubbles, including turbulent coherent structure effects on the enhancement of bubble entrainment, and bubble effects on turbulence and vorticity field. Conclusions are finally given in section 5.

2. Governing Equations

In this section, we briefly outline the numerical formulations. Details of the model may be found in Ma et al. (2011). To simulate polydisperse two-fluid flow, the dispersed bubbles are separated into NG classes or groups. Each class has a characteristic bubble diameter $d_{bi}, i = 1, 2, \cdots, NG$ and a corresponding volume fraction of $\alpha_{g,i}$. By definition, the volume fraction of all of the phases must sum to one:

$$\alpha_l + \sum_{i=1}^{NG} \alpha_{g,i} = 1 \tag{2.1}$$

where α_l is the volume fraction of liquid phase. The volume fraction of ith bubble group is related to the bubble number density $N_{g,i}$ as

$$\alpha_{g,i} = \frac{m_{g,i} N_{g,i}}{\rho_{g,i}} \tag{2.2}$$

where $m_{g,i}$ is the mass of ith bubble group, $N_{g,i}$ is number density of ith group bubble and $\rho_{g,i}$ is the bubble density.

The polydisperse bubbly flow model in the current paper is based on the analysis of Carrica et al. (1999). Similar to Moraga et al. (2008), we neglect bubble coalescence and gas dissolution. The governing equations consist of mass conservation for liquid phase,

$$\frac{\partial(\alpha_l \rho_l)}{\partial t} + \nabla \cdot (\alpha_l \rho_l \mathbf{u}_l) = 0 \tag{2.3}$$

momentum conservation for liquid phase,

$$\begin{aligned} \frac{\partial(\alpha_l \rho_l \mathbf{u}_l)}{\partial t} + \nabla \cdot (\alpha_l \rho_l \mathbf{u}_l \mathbf{u}_l) &= -\alpha_l \nabla p + \alpha_l \rho_l \mathbf{g} \\ &+ \nabla \cdot \left[\alpha_l \mu_{eff,l} (\nabla \mathbf{u}_l + \nabla^T \mathbf{u}_l)\right] + \mathbf{M}_{gl} \end{aligned} \tag{2.4}$$

bubble number density equation,

$$\frac{\partial N_{g,i}}{\partial t} + \nabla \cdot (\mathbf{u}_{g,i} N_{g,i}) = B_{g,i} + S_{g,i} + D_{g,i} \quad i = 1, \cdots, NG \tag{2.5}$$

and momentum conservation for bubble phase,

$$-\alpha_{g,i} \nabla p + \alpha_{g,i} \rho_{g,i} \mathbf{g} + \mathbf{M}_{lg,i} = 0 \quad i = 1, \cdots, NG \tag{2.6}$$

where ρ_l is liquid density, $\mathbf{u}_l$ is liquid velocity, p is pressure which is identical in phases, $\mathbf{g}$ is gravity, $\mu_{eff,l}$ is the effective viscosity of liquid phase, $\mathbf{u}_{g,i}$ is bubble velocity and $S_{g,i}$

is the intergroup mass transfer which only accounts for bubble breakup in the current study. The bubble breakup model proposed by Martínez-Bazán et al. (1999a,b, 2010) is employed. $D_{g,i}$ is the turbulent diffusion coefficient for the ith bubble group. $\mathbf{M}_{gl}$ and $\mathbf{M}_{lg,i}$ are the momentum transfers between phases, which satisfy the following relationship

$$\mathbf{M}_{gl} + \sum_{i=1}^{NG} \mathbf{M}_{lg,i} = 0 \tag{2.7}$$

where

$$\mathbf{M}_{lg,i} = \mathbf{M}_{lg,i}^{VM} + \mathbf{M}_{lg,i}^{L} + \mathbf{M}_{lg,i}^{D} \tag{2.8}$$

in which the virtual mass force $\mathbf{M}_{lg,i}^{VM}$, the lift force $\mathbf{M}_{lg,i}^{L}$ and the drag force $\mathbf{M}_{lg,i}^{D}$ are modeled as

$$\begin{aligned}
\mathbf{M}_{lg,i}^{VM} &= \alpha_{g,i}\rho_l C_{VM}(\frac{D\mathbf{u}_l}{Dt} - \frac{D\mathbf{u}_{g,i}}{Dt}) \\
\mathbf{M}_{lg,i}^{L} &= \alpha_{g,i}\rho_l C_L(\mathbf{u}_l - \mathbf{u}_{g,i}) \times (\nabla \times \mathbf{u}_l) \\
\mathbf{M}_{lg,i}^{D} &= \alpha_{g,i}\rho_l \frac{3}{4}\frac{C_D}{d_{bi}}(\mathbf{u}_l - \mathbf{u}_{g,i}) \mid \mathbf{u}_l - \mathbf{u}_{g,i} \mid
\end{aligned} \tag{2.9}$$

where C_{VM} is the virtual mass coefficient with a constant value of 0.5, C_L is the lift force coefficient which is chosen as 0.5 and C_D is the drag coefficient, which is given by (Clift et al., 1978)

$$C_D = \frac{24}{Re_{g,i}}(1 + 0.15Re_{g,i}^{0.687}) \tag{2.10}$$

where $Re_{g,i}$ is bubble Reynolds number

$$Re_{g,i} = \frac{\alpha_l\rho_l \mid \mathbf{u}_l - \mathbf{u}_{g,i} \mid d_{bi}}{\mu_l} \tag{2.11}$$

2.1. *Bubble Entrainment Model*

In the above equations, $B_{g,i}$ is the ith bubble group source due to air entrainment. As pointed out by Shi et al. (2010) and Ma et al. (2011), direct numerical simulation of bubble entrainment at the scale we wish to study is infeasible. A practical way to introduce bubbles into the computation is to prescribe air bubbles in a two-fluid model using a bubble entrainment formulation (Moraga et al., 2008; Shi et al., 2010; Ma et al., 2010, 2011). In this paper, we use the bubble entrainment formulation developed by Ma et al. (2010, 2011), who correlated bubble entrainment with turbulence dissipation rate ϵ. For polydisperse bubbles, the formulation is given by

$$B_{g,i} = \frac{c_b}{4\pi}(\frac{\sigma}{\rho_l})^{-1}\alpha_l \frac{f(a_i)\Delta a_i}{\sum_{i=1}^{NG} a_i^2 f(a_i)\Delta a_i}\epsilon \tag{2.12}$$

where c_b is bubble entrainment coefficient which has to be calibrated in the simulation. σ is surface tension, a_i is the characteristic radius of each class, Δa_i is the width of each class and $f(a_i)$ is the bubble size spectrum. In the current study, we use the spectrum suggested by Deane and Stokes (2002),

$$\begin{aligned}
f(a) &\propto a^{-10/3} \quad if \quad a \geqslant 1.0mm \\
f(a) &\propto a^{-3/2} \quad if \quad a \leqslant 1.0mm
\end{aligned} \tag{2.13}$$

where $1.0mm$ is the Hinze scale.

2.2. *Turbulence Model*

The effective viscosity of the liquid phase $\mu_{eff,l}$ is composed of three contributions: the molecular viscosity $\mu_{L,l}$, the turbulent viscosity $\mu_{T,l}$ and an extra term due to bubble induced turbulence $\mu_{BIT,l}$ (Deen, 2001).

$$\mu_{eff,l} = \mu_{L,l} + \mu_{T,l} + \mu_{BIT,l} \tag{2.14}$$

The turbulent eddy viscosity is calculated by a large-eddy simulation strategy with Smagorinsky (1963) sub-grid model.

$$\mu_{T,l} = \rho_l (C_s \Delta)^2 |\mathbf{S}| \tag{2.15}$$

where C_s is a model constant with a value of 0.1, $\mathbf{S} = \sqrt{2S_{ij}S_{ij}}$ is the characteristic filtered rate of strain, S_{ij} is the resolved strain rate and $\Delta = (\Delta x \Delta y \Delta z)^{1/3}$ is the filter width.

The bubble induced turbulent viscosity is calculated by the model proposed by Sato and Sekoguchi (1975)

$$\mu_{BIT,l} = \rho_l C_{\mu,BIT} \sum_{i=1}^{NG} \alpha_{g,i} d_{bi} |\mathbf{u}_{r,i}| \tag{2.16}$$

where the model constant $C_{\mu,BIT}$ is equal to 0.6. $\mathbf{u}_{r,i}$ is the relative velocity between bubble phase and liquid phase.

The turbulent dissipation rate ϵ is used in both bubble entrainment model and bubble breakup model. Following van den Hengel et al. (2005), the turbulent dissipation rate is estimated on the basis of the turbulent viscosity.

$$\epsilon = \frac{2\nu_{T,l}^3}{(C_s \Delta)^4} \tag{2.17}$$

in which $\nu_{T,l} = \mu_{T,l}/\rho_l$ is the turbulent kinematic eddy viscosity.

The turbulent eddy viscosity for bubble phase $\mu_{eff,g}$ is given by

$$\mu_{eff,g} = \frac{\rho_g}{Sc_g \rho_l} \mu_{eff,l} \tag{2.18}$$

where Sc_g is the Schmidt number for bubble phase which is taken equal to one.

2.3. *Free Surface Tracking*

The volume of fluid (VOF) method with second-order piecewise linear interface calculation (PLIC) scheme (Rider and Kothe, 1998) is employed to track the free surface locations. In the VOF approach, an additional equation for fluid volume fraction f is solved.

$$\frac{\partial f}{\partial t} + \nabla \cdot (\mathbf{u}_l f) = 0 \tag{2.19}$$

where f is the volume fraction of water within a computational cell. If $f = 1$, the cell is inside water, while $f = 0$, the cell is outside water, otherwise, the cell is at the air-water interface.

Details of the numerical algorithms for two-fluid equations can be found in Ma et al. (2011). During wave breaking, large-scale vortices are created on the air-side of the free surface. These vortices have high velocity, which tend to impact the Courant number and push the time step to be smaller, thus increasing the simulation costs. In the present study, we focus on the turbulent coherent structures on the water-side. Vortices on the air-side of the free surface are not considered. Therefore, we ignore the computation on the air-side. The air cells are treated as void.

2.4. *Boundary Conditions*

Boundary conditions at all physical boundaries have to be specified in order to obtain a unique solution. At the top boundary, the pressure is defined as zero. At the inlet, the volume of fluid (VOF) and velocities are specified based on the analytical solutions of cnoidal wave. Along the solid surfaces, no-slip condition is imposed. Instead of modeling every detail in the near-wall viscous sublayer region, a wall function approach is used to reduce the number of computational cells. The near-wall damping function derived by Cabot and Moin (2000) is used to approximate the kinematic eddy viscosity $\nu_t = \mu_t/\rho$ at the first cell adjacent to the wall.

$$\frac{\nu_t}{\nu} = \kappa y_w^+ (1 - exp(-y_w^+/A))^2 \tag{2.20}$$

where $y_w^+ = y_w u_*/\nu$ is the distance to the wall in wall units, $\kappa = 0.41$ and $A = 19$.

3. Numerical Simulations

In this and next sections, the numerical model is employed to study large-scale coherent structures and their effects on bubble entrainment under a surfzone spilling breaking wave. We first perform a two-dimensional simulation to assess mesh dependence of the numerical results and model's capability of simulating breaking waves. Then a three-dimensional simulation is conducted to investigate turbulence coherent structures and bubble entrainment. Our attention will be focused on evolution of coherent vortex structures and downbursts, large-scale structure effects on turbulent kinetic energy (TKE) and momentum transport as well as bubble entrainment.

3.1. *Grid Sensitivity*

Numerical study of a breaking wave is initially performed in two-dimensions without bubble effects. The main purposes of the 2D simulations are to assess mesh dependence of the numerical results and to compare with the laboratory measurements. The numerical setup follows the laboratory experiment conducted by Ting and Nelson (2011). The computational domain is 15 m long and 0.60 m deep. The beach has a slope of 0.03, with the beach toe located at 0.563 m from the left boundary. The still water depth in the constant depth region is 0.36 m. A cnoidal wave with wave height of 0.122 m and wave period of 2.0 s is incident from the left boundary.

To assess mesh dependence of the numerical results, we conducted three simulations with different grid size from $(\Delta x, \Delta z) = (0.06, 0.0075)$ down to $(\Delta x, \Delta z) = (0.02, 0.0075)$. Figure 1 displays the phase-averaged surface elevations at breaking point (5.127 m from the beach toe) with increased mesh refinement. The evolution of predicted surface elevation with different grid sizes is quite similar. However, the peak surface elevation calculated from a coarse grid $(\Delta x, \Delta z) = (0.06, 0.0075)$ is smaller than those from finer grids. The phase-averaged surface elevations with increased mesh refinement from $(\Delta x, \Delta z) = (0.04, 0.0075)$ to $(\Delta x, \Delta z) = (0.02, 0.0075)$ converge, indicating that the second-finest grid resolution $(\Delta x, \Delta z) = (0.04, 0.0075)$ is adequate for large eddy simulation of the breaking wave.

Figure 2 shows the comparison of simulated and measured wave height distribution along the beach using the grid with $(\Delta x, \Delta z) = (0.04, 0.0075)$. The simulated wave heights are determined from a segment of time series with five wave periods long. We can see that the simulated wave height compares fairly well with the measurement. Figure 3 demonstrates the comparisons of simulated and measured phase-averaged surface elevations at different locations before and after wave breaking. Again, five wave periods are

used to obtain phase-averaged surface elevations. Before wave breaking, the surface elevations are accurately predicted by the model (figure 3a,b,c). Right after wave breaking, the peak surface elevation is slightly underestimated by the model (figure 3d,e). However, as the wave propagates further onshore, the model can predict the surface elevation well again (figure 3f).

3.2. *Model Setup*

A 3D simulation has been conducted to investigate turbulent flow structures and bubble entrainment under a laboratory-scale surfzone breaking wave. The computational domain is tilted off-vertical to match bottom boundary with the $tan\beta = 0.03$ bed slope as shown in figure 4. The domain size is taken as 15 m long, 0.3 m wide and 0.6 m high, with the beach toe located at the left boundary. The still water depth at the beach toe is 0.36 m. Similar to the 2D simulation, a cnoidal wave with wave height of 0.122 m and wave period of 2.0 s is incident from the left boundary.

Before performing numerical simulations, the computational grid has to be carefully chosen. For a successful LES, we must have a filter width (Δ) in the inertial sub-range, and all scales of motion larger than Δ must be accurately resolved on the numerical grid. However, for the polydisperse two-fluid model, a basic requirement of grid resolution is that the control volume size is large enough to encompass all the interface details associated with dispersed bubbles (Dhotre et al., 2008). Milelli (2002) conducted an analysis of the minimum ratio of bubble and grid size for LES two-fluid model and came up with the criterion $\Delta/d_B > 1.5$. Based on these considerations and the mesh dependence study in 2D simulation, a uniform grid with $(\Delta x, \Delta y, \Delta z) = (0.04, 0.0075, 0.0075)$ is chosen for the 3D simulation. The maximum bubble diameter is taken as 8 mm as used by Moraga et al. (2008), which ensures that the minimum ratio of the bubble and grid size ($\Delta/d_B \approx 1.6$) falls within the Milelli criteria. Bubbles are divided into $NG = 20$ groups with a logarithmic distribution of bubble sizes. The minimum bubble diameter is taken as 0.2 mm, which is consistent with the observations by Dean and Stokes (2002).

Figure 5 presents a wave breaking event after 10 wave periods. The free surface at each time frame is marked by the $f = 0.5$ isosurface. According to Battjes (1974), the breaking wave characteristics can be correlated to the surf similarity parameter $\zeta = tan\beta/\sqrt{2\pi H/gT^2}$, where $\zeta = 0.21$ for the current case, indicating that the breaking wave is characterized by a spilling/weakly plunging breaker. As shown in figure 5, the crest of the wave slightly curls over when wave breaking starts. However, the jet thrown forward from the top of the front face collapses near the crest to form a breaking wave roller, resembling a spilling/weakly plunging breaker. As wave breaks, the free surface becomes unstable. Some small-scale surface deformations with wrinkles in the longshore direction are formed. This process is known as 'small-scale breaking' (Lakehal and Liovic, 2011). Ting (2008) argued that these three-dimensional water surface deformations play a key role in the formation and evolution of turbulent coherent structures.

4. Analysis of Flow Field

4.1. *Coherent Vortical Structures*

In the past few decades, a number of vortex identification schemes have been developed, among which the λ_2 method proposed by Jeong and Hussain (1995) has been widely used in various turbulence studies. In this method, λ_2 is the second largest eigenvalue of the tensor $\mathbf{S}^2 + \mathbf{\Omega}^2$, where $\mathbf{S}$ and $\mathbf{\Omega}$ are the symmetric and antisymmetric parts of the velocity gradient tensor $\nabla\mathbf{u}$, respectively. The interiors of vortex cores are recognized as the regions with λ_2 smaller than a negative threshold.

Figure 6 shows the evolution of instantaneous vortical structures after wave breaking, which are identified by the isosurface of $\lambda_2 = -2.0$. At the beginning of wave breaking, a small jet from the wave crest consecutively spills down the front wave face (figure 5a-d), leading to the development of large-scale spanwise vortices (figure 6a,b). These spanwise vortices are primarily located at the wave front, specifically in the roller region. After a short period of time, some vortical structures under the wave roller start developing (figure 6b,c). These vortical structures are mainly in vertical direction, with inclinations to streamwise direction. The mechanisms that induce the development of these vortical structures is postulated to be correlated with downbursts of turbulent fluid (Ting, 2008), which will be discussed later. As the breaking wave propagates further onshore to shallower region, some vortical structures oriented primarily in streamwise direction show up behind the wave crest. These streamwise vortices which are characterized as counter-rotating vortices are well-known as obliquely descending eddies (Nadaoka et al., 1989). Due to the constraint imposed by the presence of the bed, these descending eddies tend to diverge when approaching the bottom and form elongated shapes.

To investigate the characteristics of turbulent vortical structures, we conducted a statistical study of vortex inclination angles (Moin and Kim, 1985; Yang and Shen, 2009). The two-dimensional inclination angles of the streamwise direction to the projections of the vorticity vector in (x, y) and (x, z) planes are defined as $\theta_{xy} = tan^{-1}(\omega_y/\omega_x)$ and $\theta_{xz} = tan^{-1}(\omega_z/\omega_x)$, respectively. The sign convention for the angles is given in figure 7. The statistics of the inclination angles are weighted by the magnitudes of the respective projected vorticity vectors (Yang and Shen, 2009). Figure 8 shows the probabilities of θ_{xy} and θ_{xz} at $t = t_b + 5/8T$ and $t = t_b + 7/8T$, where t_b is the time for initial breaking. The breaking wave is separated into two parts: upstream of the wave crest AB and downstream of the wave crest BC, so that we can see the differences of vortex structures between the upstream part and downstream part. At $t = t_b + 5/8T$, θ_{xy} in the downstream BC is concentrated around 270^o, indicative of spanwise vortices. In the upstream AB, θ_{xy} is broadly distributed, indicating the coexistence of spanwise and streamwise vorticities. In the (x, z) plane, θ_{xz} in the downstream BC is concentrated around 245^o and 65^o. The dominant vortices are relatively vertical, with an inclination to the streamwise direction. In the upstream AB, θ_{xz} has a similar distribution as the downstream, except that the probabilities of vortex angles within $0^o \sim 45^o$ and $180^o \sim 225^o$ are higher, indicative of more streamwise vortices behind the wave crest. At $t = t_b + 7/8T$, the distributions of θ_{xy} is similar to that at $t = t_b + 5/8T$. The spanwise vortices are concentrated on the wave front. However, the distributions of θ_{xz} are different. In the downstream BC, θ_{xz} is concentrated around 260^o and 80^o, indicating that the dominant vortices are more vertical than those at $t = t_b + 5/8T$. In the upstream AB, θ_{xz} is concentrated within $0^o \sim 90^o$ and $180^o \sim 270^o$ with larger probabilities in the range of $0^o \sim 45^o$ and $180^o \sim 225^o$, indicating that the streamwise vortices are dominant behind the wave crest. These results show that the vertical vortices in the downstream and streamwise vortices in the upstream of the wave crest are all strengthened as the wave propagates onshore into shallower region.

4.2. *Downburst of Turbulent Fluid*

During wave breaking, a turbulent and aerated water mass is produced when the water spills down the front of the breaking wave. A downburst is formed when this aerated water mass descends toward the bottom without a great deal of rotation (Ting, 2008). Kubo and Sunamura (2001) observed that downbursts produced more sediment movement than obliquely descending eddies. Ting (2006, 2008) conducted systematic research on

downbursts. He found that downbursts and attached counter-rotating vortices were the primary source of turbulent energy in the breaking wave field.

Following Lakehal and Liovic (2011), we interpret the spanwise averaged flow field and free surface as the organized motion. The deviation from this average is considered as the turbulent fluctuating field. This approach has been shown to be useful for wave breaking studies (Lakehal and Liovic, 2011). Therefore, the instantaneous velocity field is decomposed into two parts: $u =< u > +u^{'}$, where $< \cdot >$ represents the spanwise averaged velocity and $u^{'}$ is the fluctuating turbulent velocity. The turbulent kinetic energy is estimated as $k = 1/2(u^{'2} + v^{'2} + w^{'2})$.

Figure 9 shows the distributions of vertical velocity fluctuation $w^{'}$ and turbulent kinetic energy k in an $x-y$ plane located approximately 17 cm above the bed. Several downburst events identified as negative $w^{'}$ can be recognized, all of which are associated with high turbulent kinetic energy. A typical downburst of turbulent fluid is shown in figure 10. The core of this downburst is located at $x = 6.25\ m$ and $y = 0.17\ m$. As observed, the downburst is associated with high turbulent kinetic energy k and Reynolds stress $-u^{'}w^{'}$, and accompanied by two counter-rotating vortices with nearly equal vorticity. The core of the downburst is located at the region between these two vortices, indicating that the downburst itself does not have a lot of rotation. The highest turbulent kinetic energy and Reynolds stress are also found in the region between the vortices, whereas the vortex centers have relatively low turbulence and Reynolds stress. These features of downburst are consistent with the laboratory observations by Ting (2006, 2008), although the simulated downburst is more organized.

The 3D structure of the downburst can be found in figure 11, which demonstrates the vertical velocity fluctuation $w^{'}$ and vertical vorticity ω_z at a set of $x - y$ planes with different vertical locations. The cores of the regions with negative $w^{'}$ are nearly in the same position of the planes, indicating that the structure of downburst is relatively vertical. As the water depth increases, the downburst becomes weaker and smaller. This downburst hasn't reached the bottom yet, however, it can bring a lot of turbulent kinetic energy and Reynolds stress to the middle part of the water column. From figure 11, we can also see the evolution of the counter-rotating vortices attached to the downburst. With the water depth increasing, the vortices becomes weaker and smaller as well. Meanwhile, the distance between vortex cores becomes closer and closer. Because the vortices cannot end in the interior of the fluid (Ting, 2008), they must merge somewhere between $z = 10cm$ and $z = 13cm$. As argued by Ting (2008), these counter-rotating vortices are parts of a vortex loop extending to the free surface.

4.3. *Turbulent Kinetic Energy and Momentum Transport*

In this section, we will study the effects of coherent structures on turbulent kinetic energy (TKE) and momentum transport. Figure 12 shows the spanwise averaged TKE distributions at different phases over a single wave period. As expected, high TKE levels are persistently located at the front part of the breaking wave crest. The highest turbulence appears when the jet from the crest collapses at the front wave face (figure 12b). At $t = t_b + 5/8T$, there is a strong downward transport of TKE behind the wave crest, which is mainly attributed to the downbursts of turbulent fluid as illustrated in figure 10. As the wave propagates onshore, this high-TKE region almost remains at the entrainment location and is detached from the wave front (figure 12d). From figure 12, we also notice that the high-TKE is transported obliquely into the water column, which is correlated to the obliquely descending eddies. This feature is more clearly seen from the downward spread of high-TKE generated by the previous breaking wave event. Figure 13 demonstrates the streamwise vorticity ω_x and TKE distributions at a $y - z$ slice

($x = 8.0m$) at $t = t_b + 5/8T$, from which we can find the correlations between obliquely descending eddies and TKE transport. As shown, the high-TKE is always located at the region between the counter-rotating vortices or the outer core of the vortices, where strong downward velocities occur. Inside the vortex core, the turbulence is relatively low. The transport of high-TKE is determined by the movements of these streamwise vortices.

The turbulent coherent structure effects on momentum transport are examined by looking at the Reynolds stress distributions. Figure 14 demonstrates spatial distributions of Reynolds stress $-u^{'}w^{'}$ at four different phases after wave breaking. Notice the dark red regions represent $-u^{'}w^{'} < 0$. These regions are primarily located near the bottom, where the turbulence is seldom affected by the wave breaking. In other words, the breaking-induced Reynolds shear stress is mainly characterized by $-u^{'}w^{'} > 0$. Here we only focus on the wave breaking generated Reynolds stress. The spatial distribution of Reynolds stress is quite similar to that of TKE. The high stress is localized at the front part of wave crest. The highest level of Reynolds stress appears at the wave roller when the jet from the crest hits the front wave face as shown in figure 14b. Right behind the wave crest, there is a strong downward transport of Reynolds stress at $t = t_b + 5/8T$, which is attributed to the downburst events. The Reynolds stress can be transported down to the bottom by the downbursts. Again, the strong Reynolds stress behind wave crest remains and decays at the entrainment location as the wave propagates onshore (figure 14d). From the distributions of Reynolds stress generated by the previous breaking event, the stress is transported obliquely into the water column behind the wave crest, supporting the conclusion that the obliquely descending eddies are effective not only on the TKE transport but also on the momentum transport. This is more clearly seen in figure 13. The pattern of Reynolds stress distributed by streamwise vortices is similar to that of TKE. As with TKE, the high Reynolds stress is always located at the regions between the counter-rotating vortices or the outer core of the vortices, where strong downward velocities occur. However, the Reynolds stress seems to be transported slightly deeper into the water column by the obliquely descending eddies.

4.4. *Bubble Entrainment*

In this section, we examine the effects of turbulent coherent structures on bubble entrainment and downward spread. Figure 15 shows the spanwise averaged void fraction distributions at four phases in a wave breaking event. In our model, bubble entrainment at the surface is correlated to the turbulent dissipation rate ϵ, which must be greater than a critical value to trigger bubble entrainment. This primarily happens in the surface roller associated with wave breaking. As shown in figure 15, the high void fractions are consistently located at the roller region of the breaking wave front. Quantitatively, the void fractions in this region fall in the range of $0.2 \sim 0.4$, which is consistent with laboratory experiments, for example, Lamarre and Melville (1991) or Cox and Shin (2003). As bubbles are entrained into the water column, a bubble plume is formed under the free surface of the wave front. This bubble plume tends to be spread backward as shown in figure 15b, indicating that the plume moves slower than the breaking wave, consistent with the 2D simulations (Ma et al., 2011). Figure 15c demonstrates that the bubble plume is further spread seaward, and subsequently downward. The oblique downward spread of bubble plume is correlated with the obliquely descending eddies and downbursts of turbulent fluid behind wave crest. It is also noticed that the bubble plume pattern is quite similar to that of turbulent kinetic energy (TKE) presented in figure 12, indicating that the mixing mechanism of dispersed bubbles is closely related to the subsurface production, transport and diffusion of turbulence, as found by Lakehal and Liovic (2011). The primary bubble plume tends to be detached from the wave front as

the breaking wave propagates onshore (figure 15d). These bubbles are trapped by the vortex structures, which will be discussed later. At this phase, the bubble plume will slowly disperse as bubbles rise to the surface. In the figure, we also notice the bubbles generated by the previous wave breaking event, which are transported obliquely into the water column. This result indicates that obliquely descending eddies have great effects on bubble entrainment and dispersion. This conclusion is further supported by figure 13, which shows the connection between obliquely descending eddies (streamwise vortices) and void fraction distribution at a $y-z$ slice at $x = 8.0m$. Similar to TKE and Reynolds stress, the bubbles are mainly transported downward at the region between the counter-rotating vortices or the outer core of the vortices, where has strong downward velocities. However, the bubbles can be trapped into the core of the streamwise vortices, which is different from the TKE and Reynolds stress. This is due to the preferential accumulation or clustering of bubbles by the vorticity field (Aliseda and Lasheras, 2011).

The effects of turbulent vortex structures on bubble transport and dispersion is also shown in the 3D plots of figure 16. The vortex structures are the same as those in figure 6, but represented by a stricter criterion $\lambda_2 = -5.0$. The void fraction distributions are recognized by the isosurfaces of $\alpha = 0.01\%$, which is mostly contributed by small bubbles. A strong downward transport of bubbles right behind the wave crest is found at $t = t_b + 5/8T$. This relatively vertical downward transport of bubbles is attributed to the downbursts of turbulent fluid, which will be presented in figure 19. Another efficient way to transport bubbles into the water column is through the obliquely descending eddies. As shown in figure 16, the bubble concentration is always high along the vortex structures. This is more clearly observed in figure 17, which displays the instantaneous flow field v and w, streamwise vorticity ω_x and void fraction α distributions at $y-z$ slices demonstrated in figure 15 at $t = t_b + 5/8T$ and $t = t_b + 7/8T$. Similar to that shown in figure 13, the high concentration of bubbles is located at the regions between the counter-rotating vortices and the outer core of the vortices, where strong downward velocities occur. These strong downward flows can counteract buoyancy force, transporting bubbles downward into the water column. The bubbles are able to be trapped into the vortex core due to the preferential accumulation. At $t = t_b + 5/8T$, four pairs of counter-rotating vortices attached to the free surface can be recognized, all of which are involved in entrainment of bubbles with high void fractions. At $t = t_b+7/8T$, vortices are transported downward to the middle of the water column, which is accompanied by the downward transport of bubbles. The strong vortex located at the left bottom corner traps large volumes of bubbles near the bottom, which corresponds to the bubble plume shown in figure 15d and 16d.

The turbulent transport of dispersed bubbles represented by $-w^{'}\alpha^{'}$ (α is the void fraction) is displayed in figure 18. As expected, the distributions of turbulent transport of bubbles is quite similar to that of void fraction. The strongest downward transport of bubbles occurs in the roller region at $t = t_b + 3/8T$, when the small jet thrown forward from the wave crest hits the front face. Behind the wave crest, bubbles are initially transported seaward parallel to the free surface (figure 18b) due to the obliquely descending eddies, and then have a strong downward transport (figure 18c), which is partly attributed to the downbursts of turbulent fluid. This is supported by figure 19, which shows bubble transport in a downburst event at $t = t_b+5/8T$. The bubble transport associated with downburst is much stronger than the neighboring regions, indicating that the downburst is efficient in downward transport of dispersed bubbles. At $t = t_b + 7/8T$, the downward transport of bubbles is becoming weaker. The bubbles start rising back to the free surface, and bubble plume disperses with void fraction decaying.

5. Discussions

5.1. *Vortex Stretching and Bending*

In the previous section, we have shown that the model is able to simulate the generation of streamwise vortices behind the wave crest of breaking waves. However, it is still debatable how these streamwise vortices are generated during wave breaking processes. Nadaoka et al. (1989) suggested that the formation and evolution of the obliquely descending eddies are related to the stretched velocity field around the saddle point of streamlines between adjacent spanwise vortices. Watanabe et al. (2005) conducted a LES study of plunging and spilling breaking waves and suggested that the mechanism for the development of streamwise vortices in breaking waves is similar to that in a mixing layer as proposed by Lasheras and Choi (1988). They argued that the obliquely descending eddies are essentially counter-rotating streamwise vortices, which are vortex loops produced by stretching and bending of perturbed vorticity in the saddle region between the rebounding jet and the primary spanwise vortex. As these streamwise vortices continue developing, a so-called rib structure is formed, involving the vortex loops wrapping around the adjacent spanwise vortices. These vortices could intertwine and entangle together to form a complex vorticity field. However, Ting (2006, 2008) questioned the similarity of the mechanism for the generation and evolution of vortex structures in a breaking wave and a mixing layer, as the breaking wave is strongly influenced by gravity which is of minor importance for a mixing layer. Moreover, the primary spanwise vortices maintained their two-dimensionality during the formation of secondary streamwise vortices (Lasheras and Choi, 1988), which is not the case in breaking waves (Ting, 2008). Ting (2006, 2008) observed in the laboratory experiments that three-dimensional water surface deformations during wave breaking play a key role in the formation and evolution of counter-rotating vortices. Ting (2008) speculated that the counter-rotating vortices are produced by stretching and bending of primary spanwise vortex structures generated in the wave breaking process, as a result of non-uniform breaking in the transverse direction. The counter-rotating vortices are then carried downward by downburst, which is associated with falling water from the broken wave. These counter-rotating vortices are further subject to stretching and bending to form obliquely descending eddies.

To understand how vortex structures evolve under breaking waves, we now study the enstrophy transport equation to quantitively investigate the effects of vortex stretching and bending on the vortex evolution processes. The equation for enstrophy transport is given by

$$\frac{D(\frac{1}{2}\omega_i\omega_i)}{Dt} = \omega_i\omega_j\frac{\partial u_i}{\partial x_j} + \nu\frac{\partial^2(\frac{1}{2}\omega_i\omega_i)}{\partial x_j\partial x_j} - \nu\frac{\partial\omega_i}{\partial x_j}\frac{\partial\omega_i}{\partial x_j} \tag{5.1}$$

where D/Dt is the material derivative, and the terms on the right hand side represent, from left to right, the stretching and bending terms, viscous diffusion and viscous dissipation for enstrophy, respectively.

The stretching and bending term determines whether there is an increase due to stretching or a decrease due to compression of enstrophy by the combination of the

signs of ω_i, ω_j and $\frac{\partial u_i}{\partial x_j}$. It includes nine-components, which are given by

$$\begin{aligned}\omega_i\omega_j\frac{\partial u_i}{\partial x_j} =& \underbrace{\omega_x\omega_x\frac{\partial u}{\partial x}}_{\Gamma_{11}} + \underbrace{\omega_x\omega_y\frac{\partial u}{\partial y}}_{\Gamma_{21}} + \underbrace{\omega_x\omega_z\frac{\partial u}{\partial z}}_{\Gamma_{31}} + \\ & \underbrace{\omega_y\omega_x\frac{\partial v}{\partial x}}_{\Gamma_{12}} + \underbrace{\omega_y\omega_y\frac{\partial v}{\partial y}}_{\Gamma_{22}} + \underbrace{\omega_y\omega_z\frac{\partial v}{\partial z}}_{\Gamma_{32}} + \\ & \underbrace{\omega_z\omega_x\frac{\partial w}{\partial x}}_{\Gamma_{31}} + \underbrace{\omega_z\omega_y\frac{\partial w}{\partial y}}_{\Gamma_{32}} + \underbrace{\omega_z\omega_z\frac{\partial w}{\partial z}}_{\Gamma_{33}}\end{aligned} \tag{5.2}$$

where each row on the right hand side accounts respectively for the rate of change in the $(\frac{1}{2}\omega_x\omega_x)$, $(\frac{1}{2}\omega_y\omega_y)$ and $(\frac{1}{2}\omega_z\omega_z)$ components of the total enstrophy due to stretching and compression of vortices.

We analyze each term in equation 5.2 by a zonal averaging approach (Lakehal and Liovic, 2011) to identify the vortex evolution processes. The breaking wave is separated into two zones: upstream zone AB and downstream zone BC, which are shown in figure 8. Figure 20 shows the zonal averaged stretching and bending terms at $t = t_b + 5/8T$. At the downstream zone BC, the vortex stretching and bending mainly happens in the upper part of the water column, primarily above the still water level. For the streamwise component $(\frac{1}{2}\omega_x\omega_x)$, Γ_{11} and Γ_{31} are positive, while Γ_{21} is negative, indicating that the streamwise component of enstrophy is increased by the vortex stretching in streamwise direction and vortex bending from the vertical vortices, but decreased by the spanwise vortices. For the vertical component $(\frac{1}{2}\omega_z\omega_z)$, Γ_{23} is positive while both Γ_{13} and Γ_{33} are negative, indicating that the vortex bending from the spanwise vortices will increase the vertical component of enstrophy, and the vortex bending from streamwise vortices and vortex stretching in vertical direction will decrease it. These results indicate that, at the wave front, the vertical vortices mainly gain energy from the primary spanwise vortices, and the streamwise vortices mainly gain energy from vertical vortices and vortex stretching. At the upstream zone AB, the vortex evolution processes are more complicated. The strongest evolution of vortices occurs in the middle of water column, where the streamwise vorticity is strengthened by the vortex stretching and bending from vertical vortices, and the vertical vortices are mainly strengthened by the bending from spanwise vortices. However, the vortex evolution processes are different in the upper part of the water column. The streamwise component of enstrophy is increased by Γ_{11} and Γ_{21}, indicating that the streamwise vortices are strengthened by the vortex stretching and bending from spanwise vortices. The vertical component of enstrophy is increased by Γ_{13} and Γ_{33}, indicating that the vertical vortices mainly gain energy from vortex stretching in the vertical direction and vortex bending from streamwise vortices.

Figure 21 shows the zonal averaged vortex stretching and bending terms at $t = t_b + 7/8T$. At the downstream zone BC, the vortex evolution processes are the same as those at $t = t_b + 5/8T$. The streamwise vortices mainly gain energy from vortex stretching in streamwise direction and vortex bending from vertical vortices. The vertical vortices gain energy from the vortex bending from the primary spanwise vortices. At the upstream zone AB, the vortex evolution mechanisms are similar all over the water column, which is different from that at $t = t_b + 5/8T$. It's perhaps because the wave breaking ceases at this phase. The vortex evolution processes are similar to that at the upwind zone. The streamwise vorticity is strengthened by the vortex stretching and vortex bending from

the vertical vortices, and the vertical vorticity is strengthened by the vortex bending from the spanwise vortices.

From the above analysis, the following conclusion can be drawn. The vortex stretching and bending plays an important role in the generation of streamwise vortices or obliquely descending eddies. The dominant mechanism of vortex evolution processes is that vertical vortices are produced by the bending of primary spanwise vortices. These vertical vortices are further subject to vortex stretching and bending to generate streamwise vortices. This conclusion is consistent with that spectulated by Ting (2008). Of course, there also exists the possibility that the streamwise vortices are directly evolved from spanwise vortices behind the wave crest during wave breaking. This mainly happens in the upper part of water column behind the wave crest, where the free surface may affects vortex evolution processes.

5.2. *3D Effects on Bubble Entrainment*

In the above sections, we have shown that the turbulent coherent structures play an important role in bubble entrainment and downward dispersion. Then a question may rise. Are bubbles transported deeper with the effects of turbulent coherent structures? To answer this question, we conducted a 2D simulation with bubbles. The model setup is the same as that in 3D simulation except that only one computational cell is chosen in the spanwise direction. Figure 22 shows the void fraction distributions from the 2D simulation at different phases after wave breaking. As we can see, it is significantly different from the spanwise-averaged void fraction distributions of the 3D simulation (figure 15). The free surface fluctuates more in the 2D simulation due to the lack of surface wrinkles in the spanwise direction and the lack of conversion of horizontal spanwise eddies to 3D vortex structures. The void fractions are restricted in the regions close to the fluctuating surfaces. Apparently, both offshore and downward dispersions of bubbles are weakened. These differences are primarily attributed to the effects of 3D turbulent coherent structures, which may transport bubbles offshore and more deeply into the water column.

5.3. *Bubble Effects on Turbulence and Vorticity Field*

Another question we may pose is that how bubbles affect turbulence and vorticity field. As found in our previous study (Ma et al., 2011), the presence of bubbles can suppress liquid phase turbulence and alter its vertical distribution. In order to further confirm this conclusion, we performed a 3D simulation without bubbles. Figure 23a presents the comparisons of zonal averaged turbulent kinetic energy with and without bubble effects at $t = t_b + 5/8T$. The zone used to do averaging covers the whole wave length (zone AC shown in figure 8). The turbulent kinetic energy and void fraction are set to zero in the air side of the free surface. The zonal averaged void fraction is shown in solid-circle line in figure 23a. We can see that the bubble effects on the vertical distributions of turbulent kinetic energy are significant. In the upper part of the water column ($z \geqslant 0.13m$), the void fraction is high. The turbulent kinetic energy with bubble effects is much smaller than that without bubble effects, indicating that the turbulence is greatly suppressed by the presence of bubbles. In the lower part of the water column, the void fraction is low. The high turbulence at the upper water column has not been transported down to the lower part of the water column (figure 12c). Therefore, the bubble effects on turbulent kinetic energy at this part is not significant. This scenario is illustrated in detail by comparing the spanwise averaged turbulent velocity $\sqrt{w'^2}$ with and without bubble effects, which is shown in figure 24. In the wave roller, the turbulence is significantly suppressed by bubbles since the void fraction in this region is high (see figure 15c). Behind the wave crest, we notice a high turbulent region with bubbles (figure 24a),

which is corresponding to the bubble plume shown in figure 15c and strong downburst events shown in figure 10. Without bubble effects, the high turbulent region behind the wave crest appears more offshore. Generally, the turbulence behind wave crests is also decreased by bubbles. In addition to the turbulent kinetic energy, the bubbles can also affect vortex structures and vorticity field. Due to the complexity of the vortex structures under breaking waves, we cannot observe the bubble effects on a single vortex. Therefore, we only take a look at the vorticity field represented by the zonal averaged enstrophy $< \frac{1}{2}\omega_i\omega_i >$, which is shown in figure 23b. The bubble effect on the enstrophy is similar to that on turbulent kinetic energy. In the upper part of the water column, because the turbulence is suppressed with bubbles, the vorticity is also decreased by the presence of bubbles. In the lower part of the water column, the vorticity field is not significantly affected by bubbles since the void fraction is low. The bubble effects on the statistics of turbulent vortex structures are displayed in figure 25. Bubbles seldom influence the shape of free surface. The probability distributions of θ_{xy} with and without bubbles both show the co-existence of spanwise and streamwise vortices. Three peaks can be recognized in the distribution of θ_{xy} at the upstream part. Two peaks around 90^o and 270^o are corresponding to the spanwise vortices, while another peak around 180^o is corresponding to the streamwise vortices. We notice that bubbles rarely affect the spanwise vortices. However, they can affect the generation of streamwise vortices. This is also found in the downstream part, where the distribution of θ_{xy} peaks smaller than 270^o without bubbles, indicating that more streamwise vortices are generated without bubble effects. Because the streamwise vortices are evolved from the spanwise and vertical vortices as discussed above, these results demonstrate that bubbles may attenuate the evolution processes of turbulent vortex structures. This conclusion is further and more clearly illustrated by the probability distribution of θ_{xz}, particularly in the upstream part. With bubbles, the distribution of θ_{xz} peaks around 260^o, whereas it peaks around 180^o without bubbles, indicating that more vertical vortices are evolved into streamwise vortices without bubble effects. This occurs because the presence of bubbles suppresses turbulence, and subsequently attenuates vortex evolution processes.

6. Conclusions

A large-eddy simulation of polydisperse bubbly flow under a surfzone spilling breaking wave was performed to investigate the interactions between turbulent coherent structures and bubble entrainment. The numerical model, solving the two-phase (gas-liquid) flow equations with volume-of-fluid (VOF) surface tracking scheme and Smagorinsky subgrid turbulence closure, explicitly accounts for dispersed bubble effects on momentum and turbulence in the liquid phase as well as turbulent transport on dispersed bubbles. The model was shown to predict free surface evolution and wave height distribution fairly well in a laboratory-scale surfzone, and was capable of capturing large-scale turbulent coherent structures such as obliquely descending eddies (streamwise vortices) and downbursts of turbulent fluid under breaking waves.

The numerical model was then utilized to study turbulent coherent structure effects on turbulent kinetic energy and momentum transport as well as bubble entrainment. The results showed that the downburst of turbulent fluid is efficient on the downward transport of TKE and Reynolds stress. The obliquely descending eddies also play an important role on TKE and momentum transport. The high levels of TKE and Reynolds stress are always located at the regions between the counter-rotating vortices or the outer core of the vortices, where has strong downward velocities. The effects of turbulent coherent structures on bubble entrainment are also significant. Similar to the TKE

and Reynolds stress, bubbles are also transported downward at the regions between the counter-rotating vortices. Moreover, bubbles can be trapped into the vortex core due to the preferential accumulation by the vorticity field. The coherent structures tend to transport bubbles offshore and more deeply into the water column.

The mechanisms for the generation of streamwise vortices or obliquely descending eddies were discussed by analyzing the vortex stretching and bending terms in the enstrophy transport equation. It was found that the vortex stretching and bending plays an important role in the generation of streamwise vortices. The dominant mechanism of vortex evolution processes is that vertical vortices are produced by the bending of primary spanwise vortices, which are further subject to vortex stretching and bending to generate streamwise vortices. This finding is consistent with that speculated by Ting (2008). We also discussed the bubble effects on turbulence and vorticity field. It was found that both turbulent kinetic energy and enstrophy are decreased by the presence of bubbles. The evolution processes of turbulent vortex structures are attenuated as well.

Acknowledgments: This study was supported by Office of Naval Research, Coastal Geosciences Program under grants N00014-09-1-0088 and N00014-10-1-0088.

REFERENCES

Aliseda, A. & Lasheras, J. C. 2011 Preferential concentration and rise velocity reduction of bubbles immersed in a homogeneous and isotropic turbulent flow, *Phys. Fluids* **23**, 093301, doi: 10.1063/1.3626404

Battjes, J. A. 1974 Surf similarity, *Proc. 14th Coastal Engrg. Conf.*, ASCE, New York, 466-480

Buscaglia, G. C., Bombardelli, F.A. & Garcia, M. H. 2002 Numerical modeling of large-scale bubble plumes accounting for mass transfer effects, *Int. J. Multiphase Flow*, **28**, 1763-1785

Cabot, W. & Moin, P. 2000 Approximate wall boundary conditions in the large-eddy simulation of high Reynolds number flow, *Flow Turb. Combust.*, **63**, 269-291

Carrica, P. M., Drew, D. A., Bonetto, F. & Lahey, R.T. Jr. 1999 A polydisperse model for bubbly two-phase flow around a surface ship, *Int. J. Multiphase Flow*, **25**, 257-305

Chang, K.-A. & Liu, P.L.-F. 1998 Velocity, acceleration and vorticity under a breaking wave, *Phys. Fluids*, **10**, 327-329

Chang, K.-A. & Liu, P.L.-F. 1999 Experimental investigation of turbulence generated by breaking waves in water of intermediate depth, *Phys. Fluids*, **11**, 3390-3400

Christensen, E. D. & Deigaard, R. 2001 Large eddy simulation of breaking waves, *Coastal Engineering*, **42**, 53-86

Christensen, E. D. 2006 Large eddy simulation of spilling and plunging breakers, *Coastal Engineering*, **53**, 463-485

Clift, R., Viollet, k. R. & Weber M.E. 1978 Bubbles, Drops and Particles, *Academic Press*, New York, USA.

Cox, D. T. & Kobayashi, N. 2000 Identification of intensive, intermittent coherent motions under shoaling and breaking waves, *J. Geophy. Res.*, **105(C6)**, 14223-14236

Cox, D. & Shin S. 2003 Laboratory measurements of void fraction and turbulence in the bore region of surf zone waves, *J. Eng. Mech.*, **129**, 1197-1205

Dalrymple, R. A. & Rogers, B. D. 2006 Numerical modeling of water waves with the SPH method, *Coastal Engineering*, **53**, 141-147

Deane, G. B. & Stokes, M. D. 2002 Scale dependence of bubble creation mechanisms in breaking waves, *Nature*, **418**, 839-844.

Deen, N. G., Solberg, T. & Hjertager, B. H. 2001 Large eddy simulation of the gas-liquid flow in a square cross-sectioned bubble column, *Chemical Engineering Science*, **56**, 6341-6350

Dhotre, M. T., Niceno, B. & Smith, B. L. 2008 Large eddy simulation of a bubble column using dynamic sub-grid scale model, *Chemical Engineering Journal*, **136**, 337-348

Jeong, J. & Hussain, F. 1995 On the identification of a vortex, *J. Fluid Mech.*, **285**, 69-94

Kataoka, I. & Serizawa, A. 1989 Basic equations of turbulence in gas-liquid two-phase flow, *Int. J. Multiphase Flow*, **15**, 843-855

Kubo, H. & Sunamura, T. 2001 Large-scale turbulence to facilitate sediment motion under spilling breakers, *Proceedings of the 4th Conference on Coastal Dynamics*, Lund, Sweden, 212-221

Lakehal, D. & Liovic, P. 2006 Large-eddy simulation of steep water waves, *Proceedings of the IUTAM Symposium on Computational Multiphase Flow*, 331-340

Lakehal, D. & Liovic, P. 2011 Turbulent structure and interaction with surface dynamics in breaking waves, *J. Fluid Mech.*, **674**, 522-577

Lamarre, E. & Melville W. K. 1991 Air entrainment and dissipation in breaking waves, *Nature*, **351**, 469-472.

Lasheras, J. C. & Choi, H. 1988 Three-dimensional instability of a plane free shear layer: an experimental study of formation and evolution of streamwise vortices, *J. Fluid Mech.*, **189**, 53-86

Lin, P. & Liu, P.L.-F. 1998 A numerical study of breaking waves in the surf zone, *J. Fluid Mech.*, **359**, 239-264

Lin, P. & Liu, P.L.-F. 1998 Turbulence transport, vorticity dynamics, and solute mixing under plunging breaking waves in surf zone, *J. Geophy. Res.*, **103(C8)**, 15677-15694

Liu, P.L.-F., Wu, T. -R., Raichlen, F., Synolakis, C. E. & Borrero, J. C. 2005 Runup and rundown generated by three-dimensional sliding masses, *J. Fluid Mech.*, **536**, 107-144

Lopez de Bertodano, M., Lahey, R. T. Jr. & Jones, O. C. 1994 Development of a $k-\epsilon$ model for bubbly two-phase flow, *Journal of Fluids Engineering*, **116**, 128-134

Lubin, P., Vincent, S., Abadie, S. & Caltagirone, J. -P. 2006 Three-dimensional large eddy simulation of air entrainment under plunging breaking waves, *Coastal Engineering*, **53**, 631-655

Ma, G., Shi, F. & Kirby, J. T. 2010 A polydisperse two-fluid model for bubble plumes under breaking waves, *Proceedings of 7th International Conference on Multiphase Flow*, Tampa, Florida, USA

Ma, G., Shi, F. & Kirby, J. T. 2011 A polydisperse two-fluid model for surf zone bubble simulation, *J. Geophy. Res.*, **116**, C05010, doi:10.1029/2010JC006667

Martínez-Bazán, C., Montañés J. L. & Lasheras J. C. 1999 On the breakup of an air bubble injected into a fully developed turbulent flow. Part 1. Breakup frequency, *J. Fluid Mech.*, **401**, 157-182.

Martínez-Bazán, C., Montañés J. L. & Lasheras J. C. 1999 On the breakup of an air bubble injected into a fully developed turbulent flow. Part 2. Size PDF of the resulting daughter bubbles, *J. Fluid Mech.*, **401**, 183-207.

Martínez-Bazán, C., Rodrŕguez-Rodríguez, J., Deane G. B., Montañes J. L. & Lasheras J. C. 2010 Considerations on bubble fragmentation models, *J. Fluid Mech.*, **661**, 159-177.

Milelli, M. 2002 A numerical analysis of confined turbulent bubble plume, Diss. EH. No. 14799, Swiss Federal Institute of Technology, Zurich.

Moin, P. & Kim, J. 1985 The structure of the vorticity field in turbulent channel flow. Part 1. Analysis of instantaneous fields and statistical correlations, *J. Fluid Mech.*, **155**, 441-464

Moraga, F. J., Carrica, P. M., Drew, D. A. & Lahey, R. T. Jr. 2008 A sub-grid air entrainment model for breaking bow waves and naval surface ships, *Computers & Fluids*, **37**, 281-298

Nadaoka, K., Hino, M. & Koyano Y. 1989 Structure of the turbulent flow field under breaking waves in the surf zone, *J. Fluid Mech.*, **204**, 359-387

Rider, W. J. & Kothe, D. B. 1998 Reconstructing volume tracking, *J. Comput. Phys.*, **141**, 112-152

Sato, Y. & Sekoguchi, K. 1975 Liquid velocity distribution in two-phase bubble flow, *Int. J. Multiphase Flow*, **2**, 79-95.

Serizawa, A. & Kataoka, I. 1990 Turbulence suppression in bubbly two-phase flow, *Nuclear Engineering and Design*, **122**, 1-16

Shao, S. & Ji, C. 2006 SPH computation of plunging waves using a 2-D sub-particle scale (SPS) turbulence model, *Int. J. Num. Method in Fluids*, **51**, 913-936

Shi, F., Kirby, J. T. & Ma, G. 2010 Modeling quiescent phase transport of air bubbles induced by breaking waves, *Ocean Modelling*, **35**, 105-117

Smagorinsky, J. 1963 General circulation experiments with the primitive equations, *Mon. Weather Rev.*, **91**, 99-165.

Sou, I. M., Cowen, E. A. & Liu, P.L.-F. 2010 Evolution of the turbulence structure in the surf and swash zones, *J. Fluid Mech.*, **644**, 193-216

Sridhar, G. & Katz, J. 1999 Effect of entrained bubbles on the structure of vortex rings, *J. Fluid Mech.*, **397**, 171-202

Ting, F. C. K. & Kirby, J. T. 1994 Observation of undertow and turbulence in a laboratory surf zone, *Coastal Engineering*, **24**, 52-80

Ting, F. C. K. & Kirby, J. T. 1995 Dynamics of surf zone turbulence in a strong plunging breaker, *Coastal Engineering*, **24**, 177-204

Ting, F. C. K. & Kirby, J. T. 1996 Dynamics of surf zone turbulence in a spilling breaker, *Coastal Engineering*, **27**, 131-160

Ting, F. C. K. 2006 Large-scale turbulence under a solitary wave, *Coastal Engineering*, **53**, 441-462

Ting, F. C. K. 2008 Large-scale turbulence under a solitary wave: Part 2 Forms and evolution of coherent structures, *Coastal Engineering*, **55**, 522-536

Ting, F. C. K. & Nelson, J. R. 2011 Laboratory measurements of large-scale near-bed turbulent flow structures under spilling regular waves, *Coastal Engineering*, **58**, 151-172

van den Hengen, E. I. V., Deen, N. G. & Kuipers, J. A. M. 2005 Application of coalescence and breakup models in a discrete bubble model for bubble columns, *Industrial and Engineering Chemistry Research*, **44**, 5233-5245

Wang, S. K., Lee, S. J., Jones, O. C. Jr. & Lahey, R. T. Jr. 1987 3-D turbulence structure and phase distribution measurements in bubbly two-phase flows, *Int. J. Multiphase Flow*, **13**, 327-343

Watanabe, Y. & Saeki, H. 1999 Three-dimensional large eddy simulation of breaking waves, *Coastal Engineering Journal*, **41**, 281-301

Watanabe, Y., Saeki, H. & Hosking, R. J. 2005 Three-dimensional vortex structures under breaking waves, *J. Fluid Mech.*, **545**, 291-328

Wu, T. R. 2004 A numerical study of three dimensional breaking waves and turbulence effects, Ph.D dissertation, Cornell University

Yang, D. & Shen, L. 2009 Characteristics of coherent vortical structures in turbulent flows over progressive surface waves, *Phys. Fluids*, **21**, 125106, doi:10.1063/1.3275851

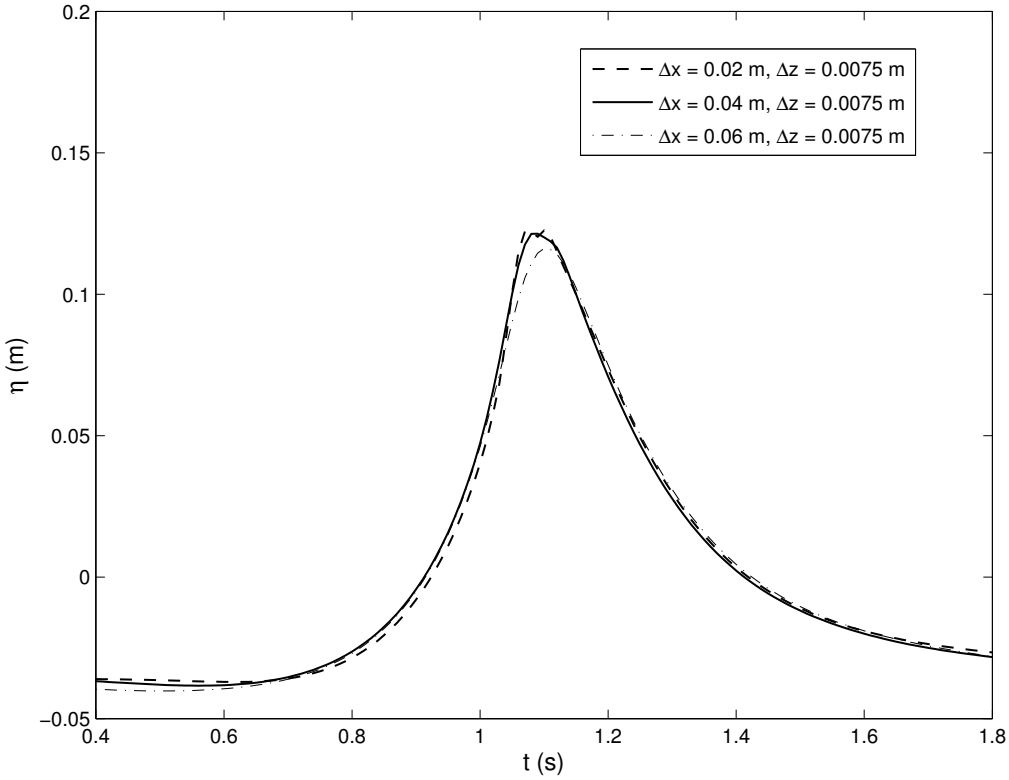

FIGURE 1. Mesh dependence of phase-averaged surface elevation at $x = x_b$. x_b (5.127 m from the beach toe) is the location of breaking point.

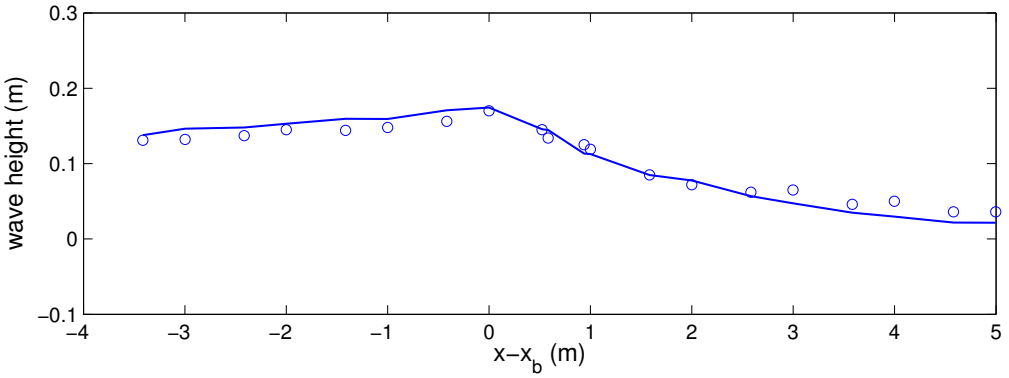

FIGURE 2. Comparisons between numerical (solid line) and experimental (circles) wave height.

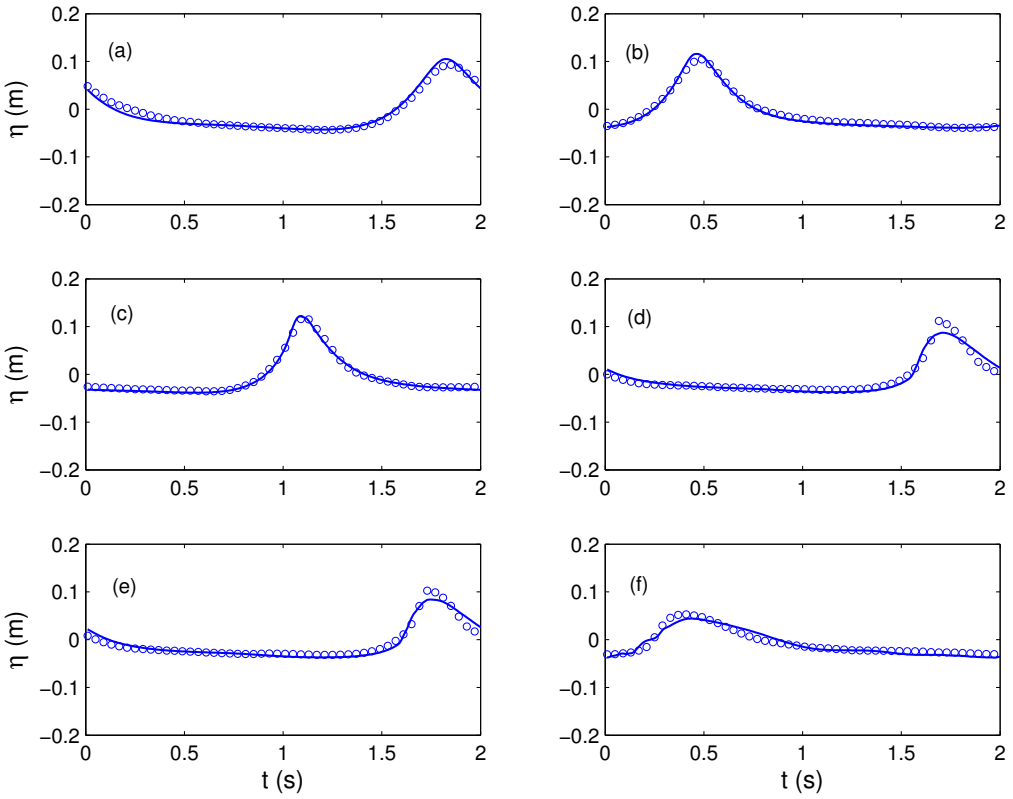

FIGURE 3. Comparisons between numerical (solid line) and experimental (circles) phase-averaged surface elevations at six wave gauges: (a) $x - x_b = -2.414\ m$; (b) $x - x_b = -1.415\ m$; (c) $x - x_b = 0.0\ m$; (d) $x - x_b = 0.938\ m$; (e) $x - x_b = 1.999\ m$; (f) $x - x_b = 3.582\ m$.

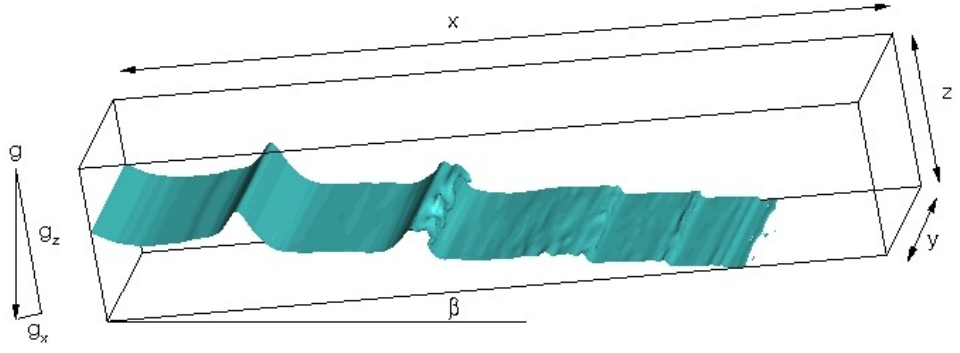

FIGURE 4. Computational domain and model setup for the spilling breaking wave. The domain size is 15 m long, 0.3 m wide and 0.6 m high. The domain boundary matches the $tan\beta = 0.03$ bed slope.

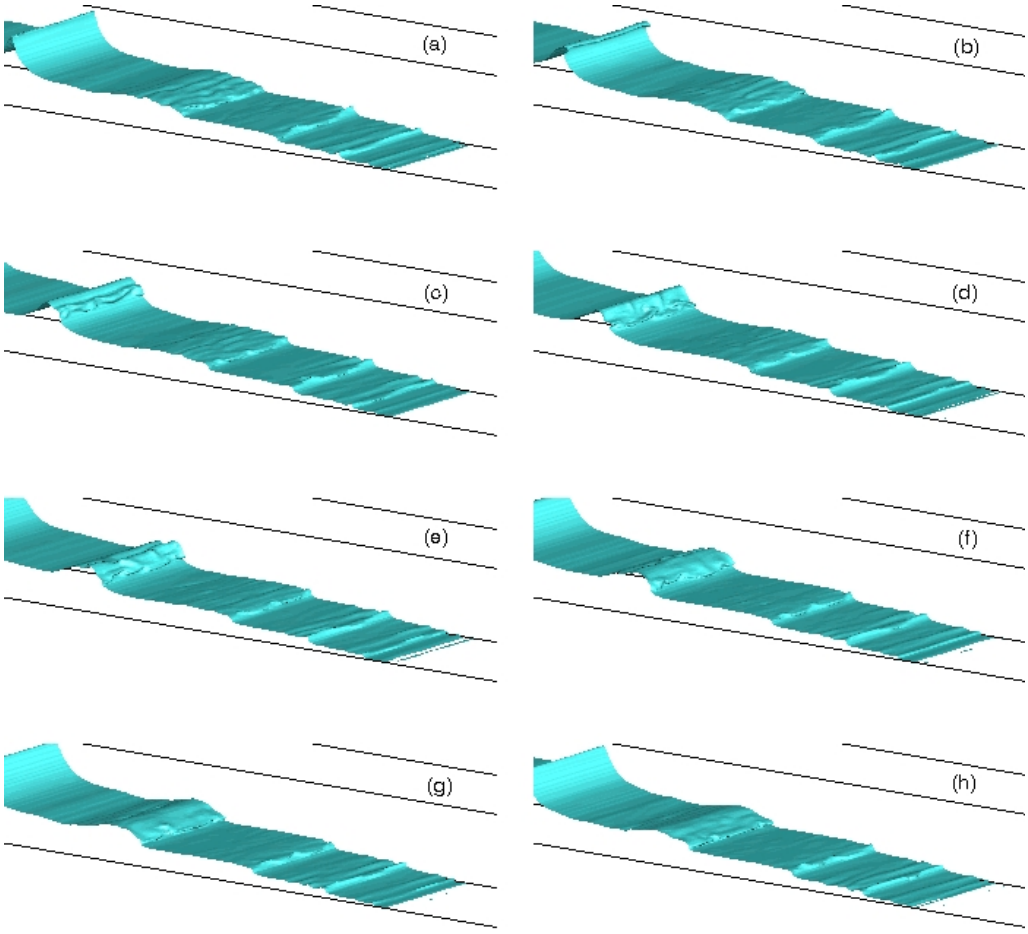

FIGURE 5. Free surface profile of a spilling breaking wave at (a) $t = t_b$; (b) $t = t_b + 1/8T$; (c) $t = t_b + 2/8T$; (d) $t = t_b + 3/8T$; (e) $t = t_b + 4/8T$; (f) $t = t_b + 5/8T$; (g) $t = t_b + 6/8T$; (h) $t = t_b + 7/8T$. t_b is time for initial wave breaking, T is wave period.

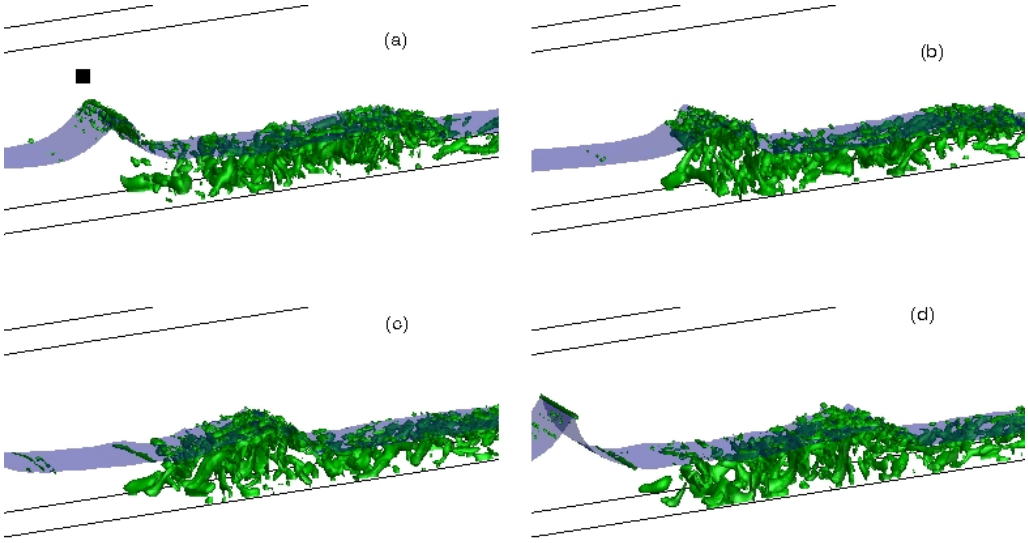

FIGURE 6. Evolution of coherent vortical structures in a spilling breaking wave at (a) $t = t_b + 1/8T$; (b) $t = t_b + 3/8T$; (c) $t = t_b + 5/8T$; (d) $t = t_b + 7/8T$. t_b is time for initial wave breaking, T is wave period. The vortical structures are identified by the isosurface of $\lambda_2 = -2.0$

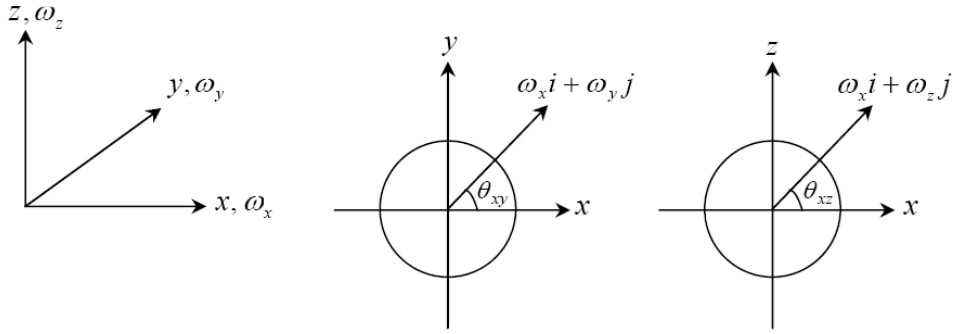

FIGURE 7. Sign convention for vorticity inclination angles θ_{xy} and θ_{xz}, where θ_{xy} is the angle from the $+x$-axis to $\omega_x\mathbf{i} + \omega_y\mathbf{j}$ in the (x, y) plane and θ_{xz} is the angle from the $+x$-axis to $\omega_x\mathbf{i} + \omega_z\mathbf{k}$ in the (x, z) plane (adapted from Yang and Shen, 2009).

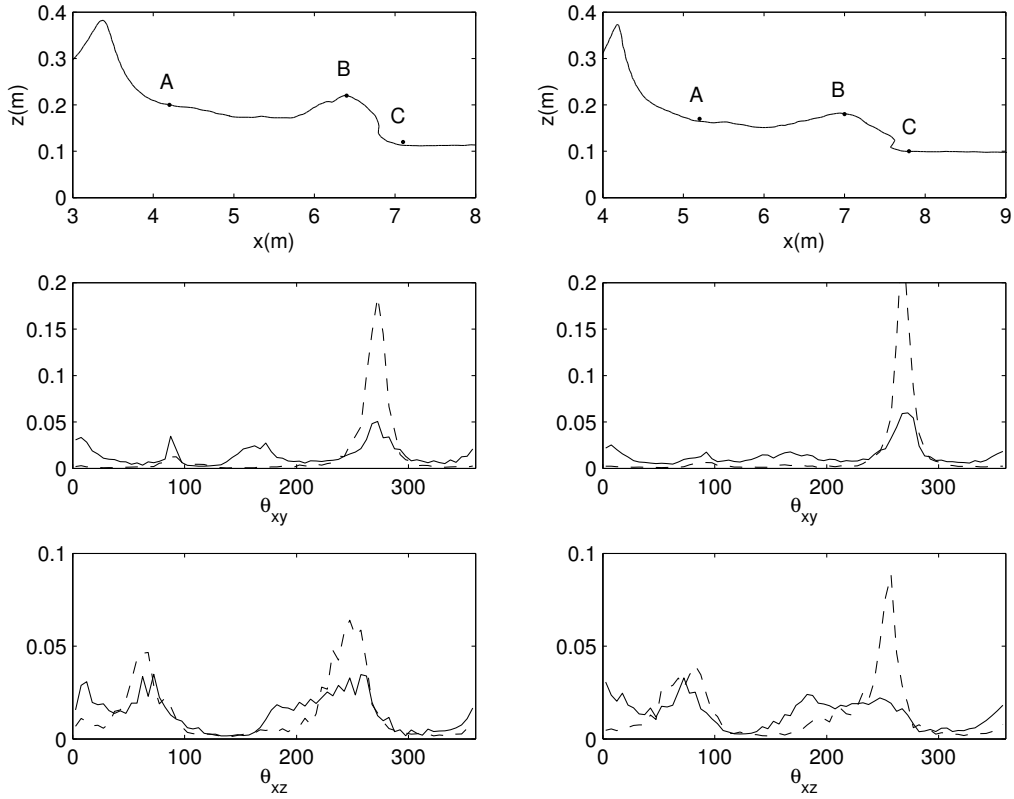

FIGURE 8. Probabilities of two-dimensional vorticity angles at the upstream AB and downstream BC of the wave crest at $t = t_b + 5/8T$ (left) and $t = t_b + 7/8T$ (right). Solid line: upstream part; dashed line: downstream part.

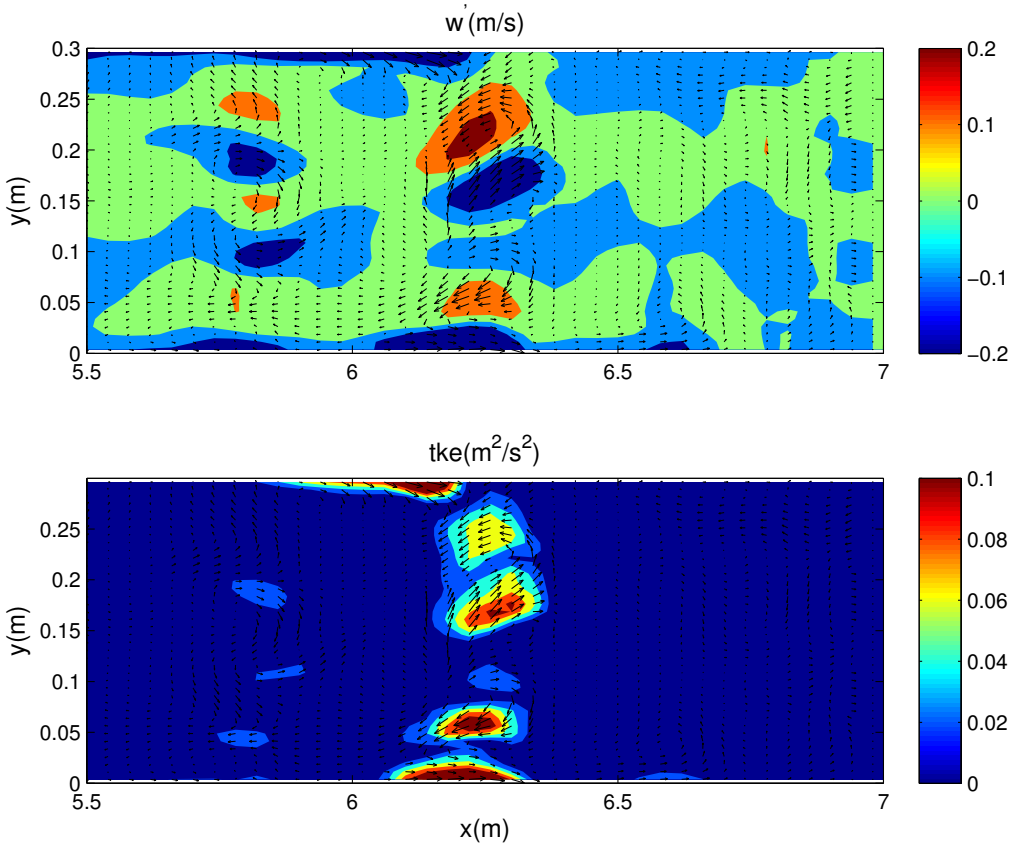

FIGURE 9. Instantaneous turbulence velocity $u^{'}$, $v^{'}$ and $w^{'}$ (in m/s) and turbulent kinetic energy $k = 1/2(u^{'2} + v^{'2} + w^{'2})$ (in m^2/s^2) at a x-y slice 17 cm above the bed at $t = t_b + 5/8T$.

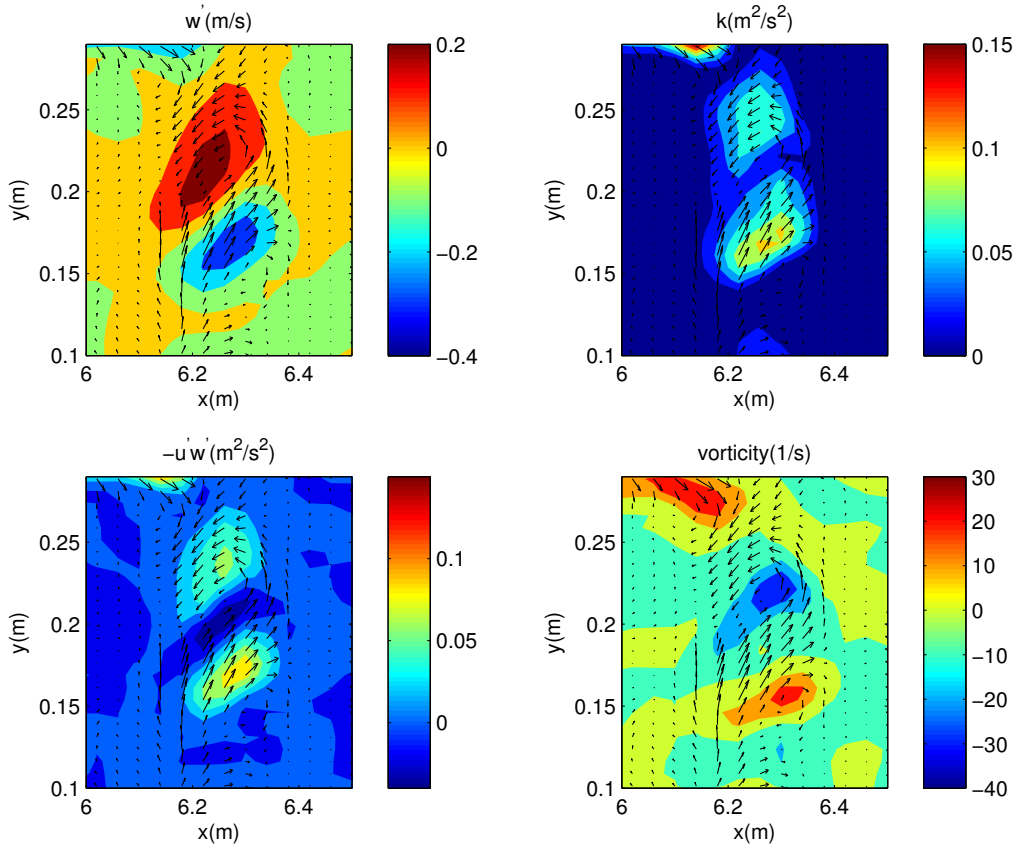

FIGURE 10. Instantaneous turbulence velocity $u^{'}$, $v^{'}$ and $w^{'}$ (in m/s), turbulent kinetic energy $k = 1/2(u^{'2} + v^{'2} + w^{'2})$ (in m^2/s^2), Reynolds stress $-u^{'}w^{'}$ (in m^2/s^2) and vorticity $du^{'}/dy - dv^{'}/dx$ (in $1/s$) from a downburst at $t = t_b + 5/8T$. The focus area is located at 17 cm above the bed.

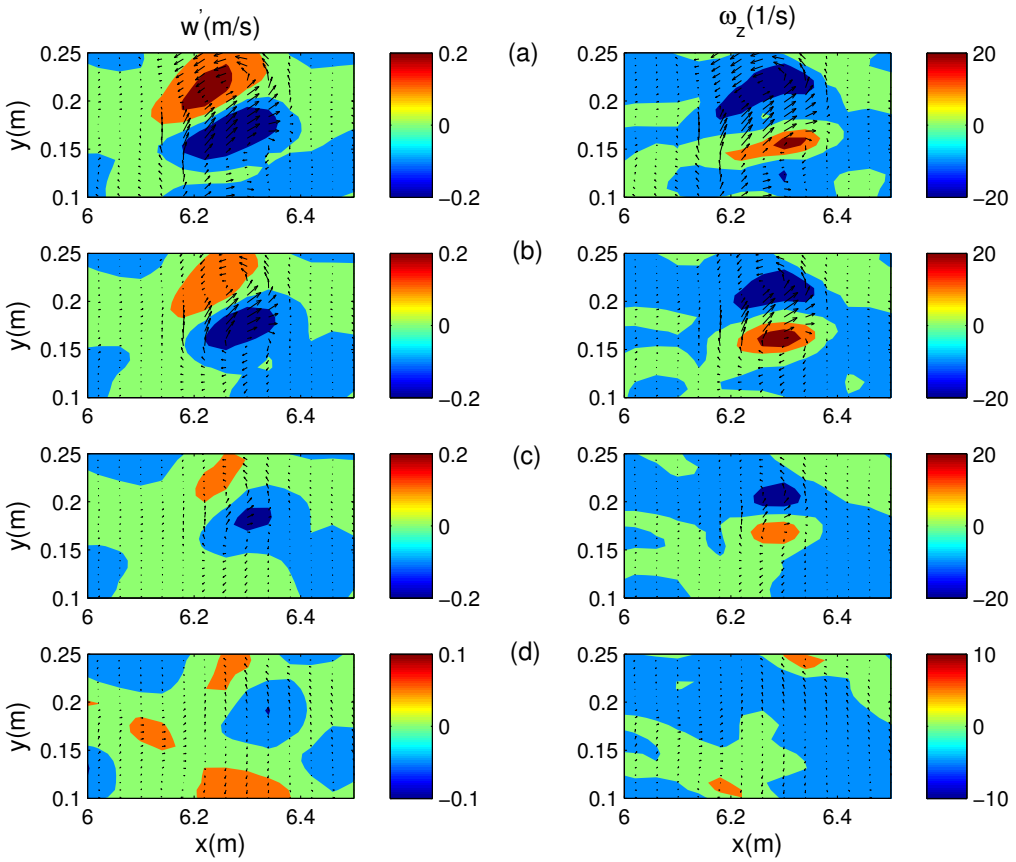

FIGURE 11. Evolution of the downburst in the vertical direction at (a) $z = 17cm$; (b) $z = 15cm$; (c) $z = 13cm$ and (d) $z = 10cm$.

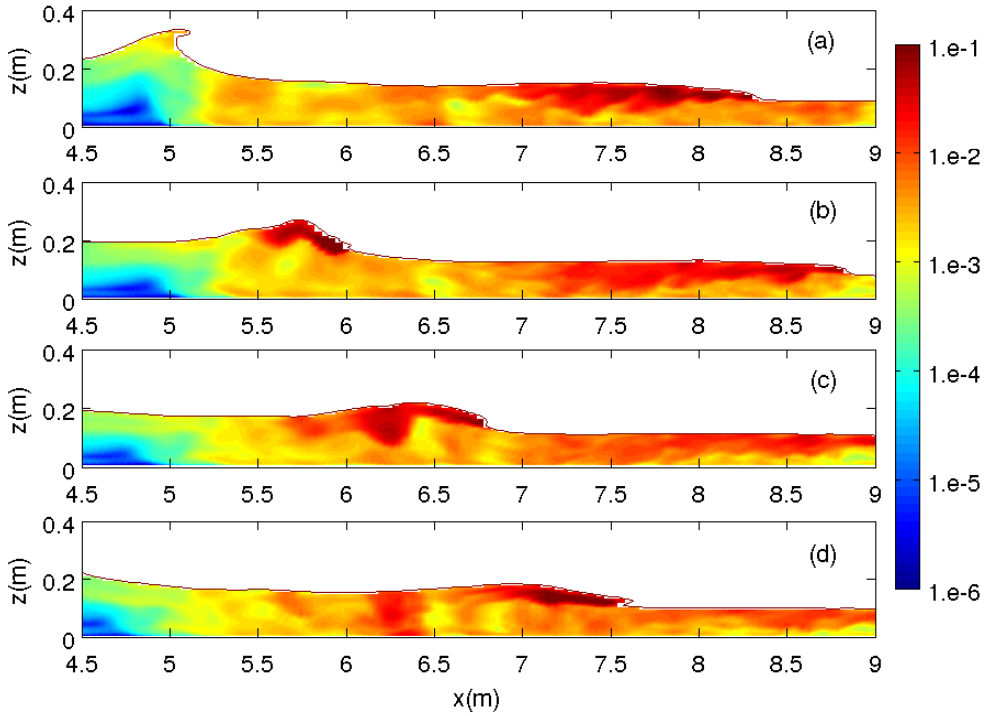

FIGURE 12. Spanwise averaged turbulent kinetic energy at (a) $t = t_b + 1/8T$; (b) $t = t_b + 3/8T$; (c) $t = t_b + 5/8T$ and (d) $t = t_b + 7/8T$.

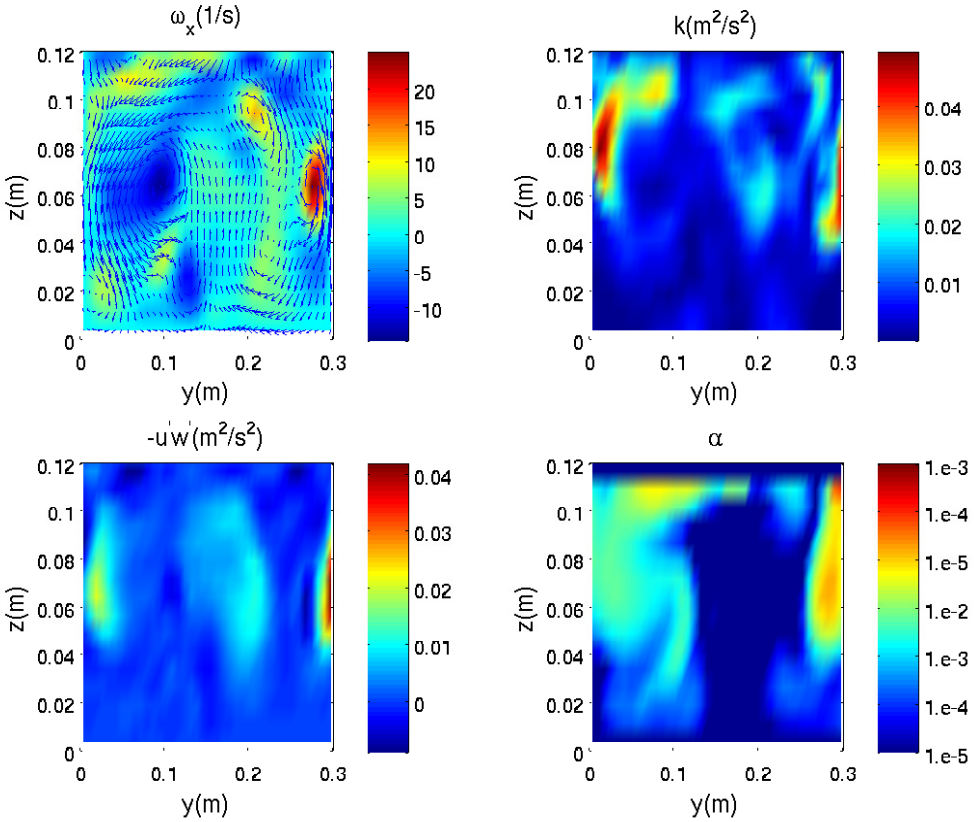

FIGURE 13. Instantaneous velocity field v and w, streamwise vorticity ω_x, turbulent kinetic energy k, Reynolds stress $-u^{'}w^{'}$ and void fraction distribution α at a $y-z$ slice ($x = 8.0m$) at $t = t_b + 5/8T$.

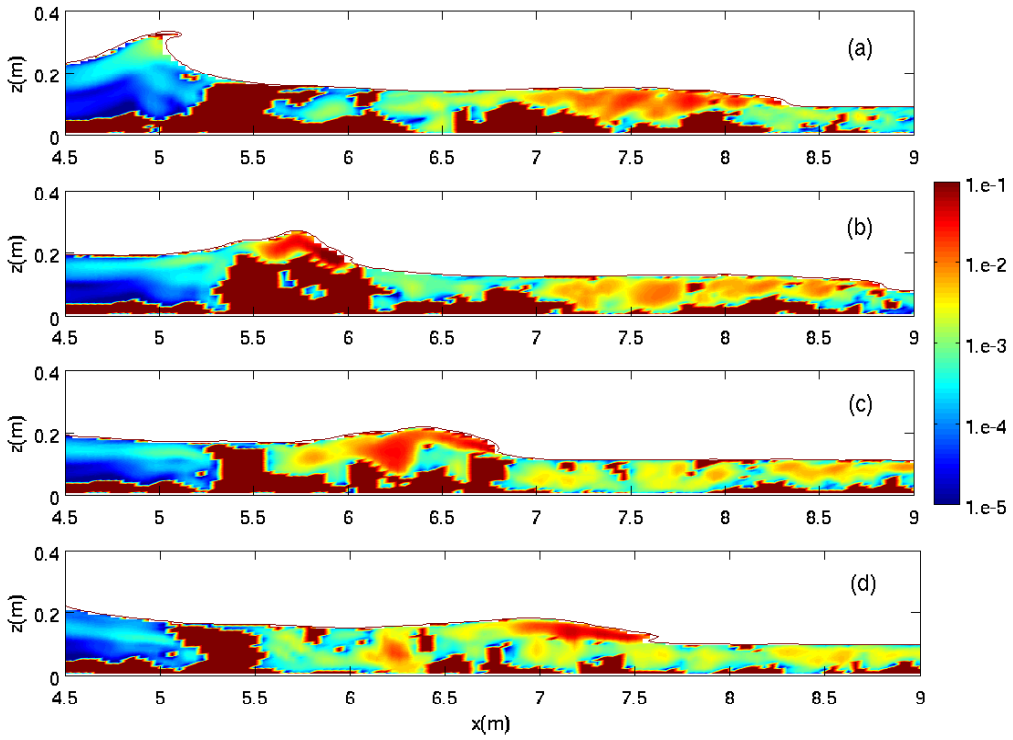

FIGURE 14. Spanwise averaged Reynolds stress $-\overline{u'w'}$ distributions at (a) $t = t_b + 1/8T$; (b) $t = t_b + 3/8T$; (c) $t = t_b + 5/8T$ and (d) $t = t_b + 7/8T$. Dark red denotes $-\overline{u'w'} < 0$.

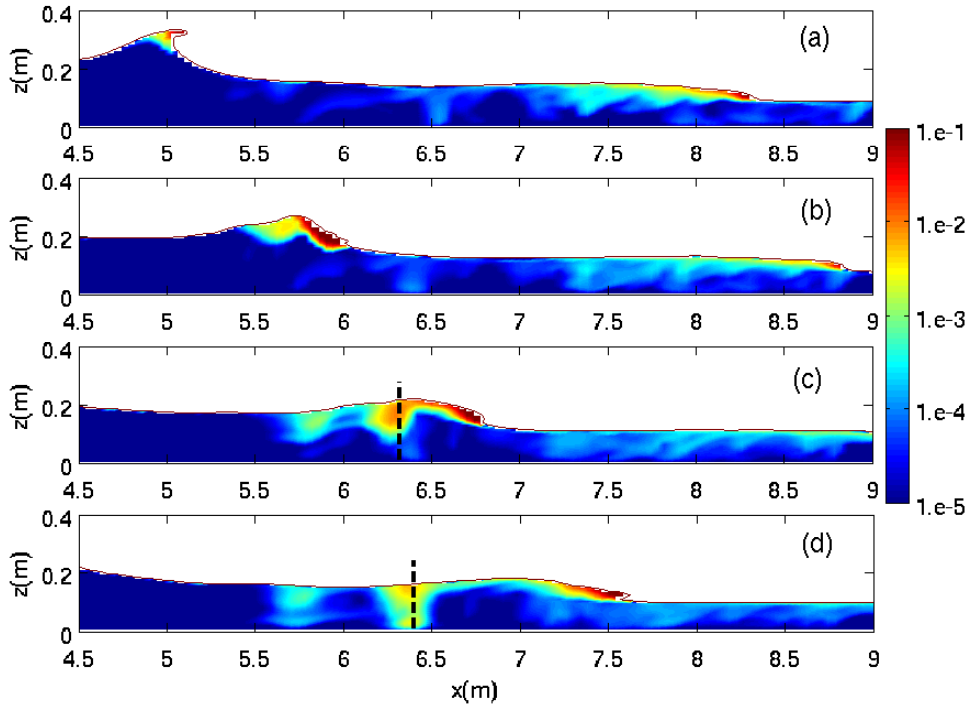

FIGURE 15. Spanwise averaged void fraction distributions at (a) $t = t_b + 1/8T$; (b) $t = t_b + 3/8T$; (c) $t = t_b + 5/8T$ and (d) $t = t_b + 7/8T$. Two dashed lines shown in (c) and (d) indicate the locations of $y - z$ slices for figure 17.

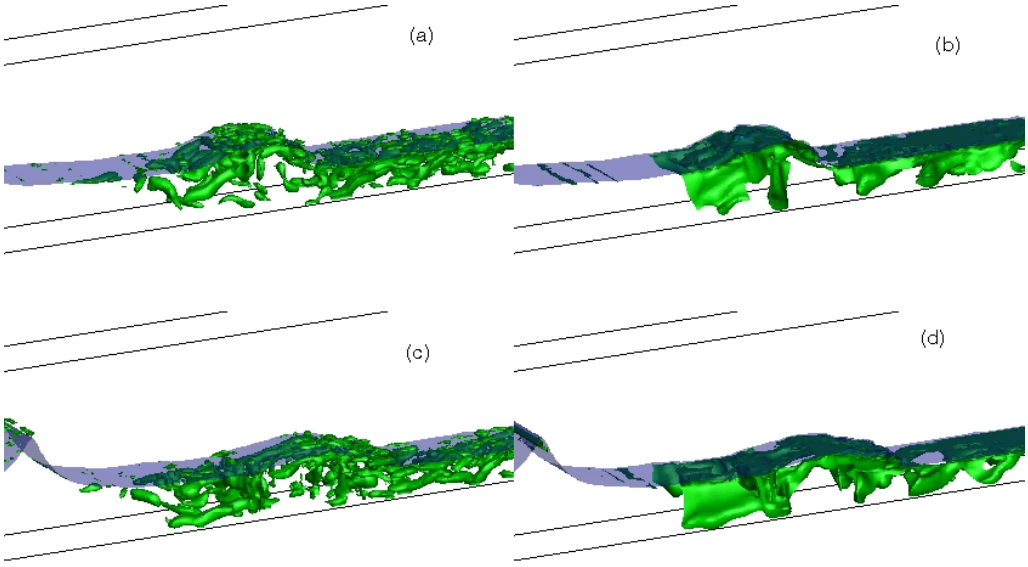

FIGURE 16. The effects of vortex structures (recognized by isosurfaces of $\lambda_2 = -5.0$) on void fraction distributions (isosurfaces of $\alpha = 0.01\%$). (a) vortex structures at $t = t_b + 5/8T$; (b) void fraction distribution at $t = t_b + 5/8T$; (c) vortex structures at $t = t_b + 7/8T$; (d) void fraction distribution at $t = t_b + 7/8T$.

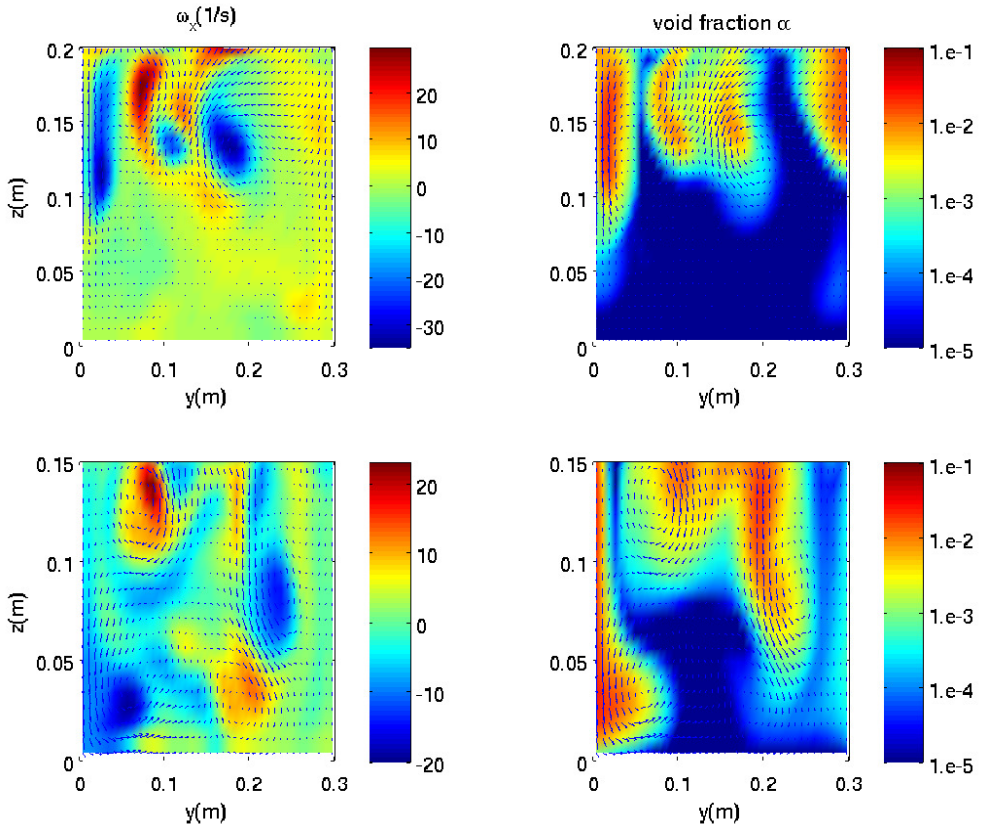

FIGURE 17. Streamwise vorticity ω_x and void fraction distribution α at $y-z$ slices as shown in figure 15 at $t = t_b + 5/8T$ (upper pannels) and $t = t_b + 7/8T$ (lower pannels).

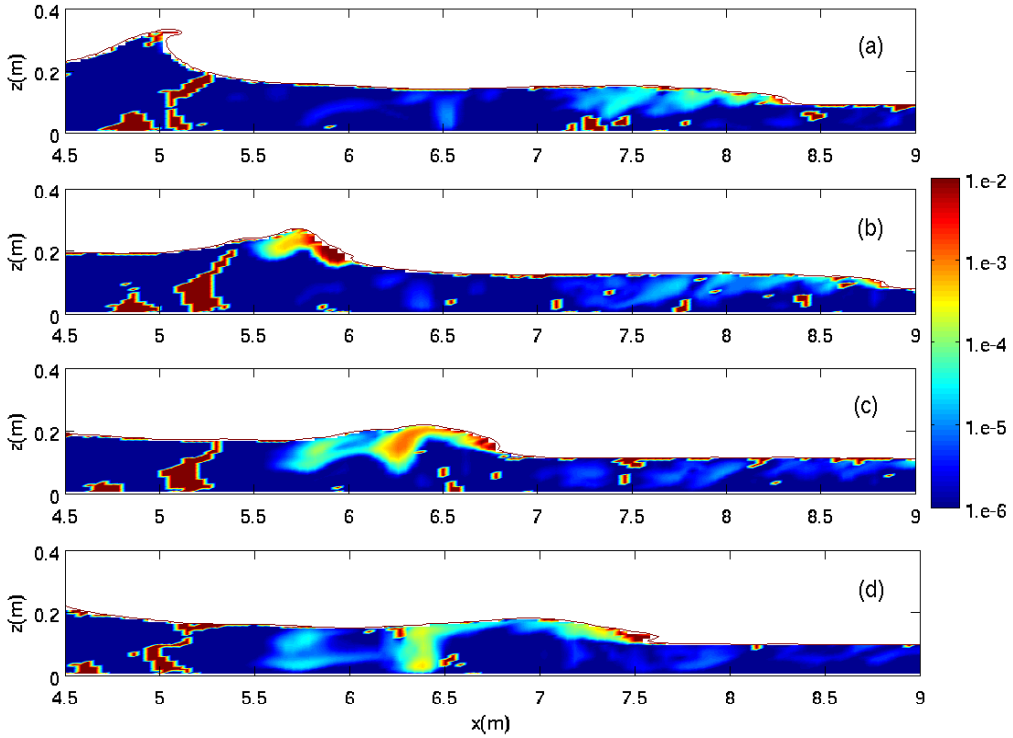

FIGURE 18. Spanwise averaged turbulent transport of bubbles $-w^{'}\alpha^{'}$ at (a) $t = t_b + 1/8T$; (b) $t = t_b + 3/8T$; (c) $t = t_b + 5/8T$ and (d) $t = t_b + 7/8T$. Dark red denotes $-w^{'}\alpha^{'} < 0$.

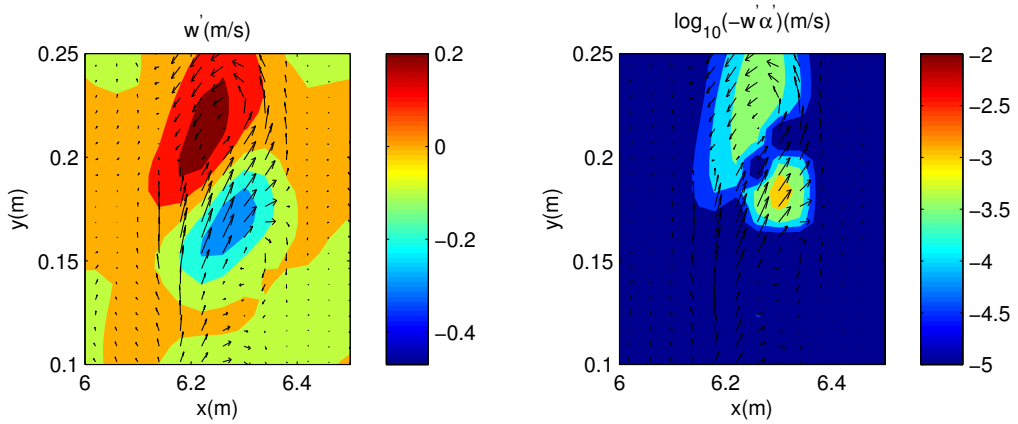

FIGURE 19. Bubble transport by a downburst event at $t = t_b + 5/8T$. The downburst is identified by negative $w^{'}$, and the bubble transport associated with the downburst are much stronger than neighboring regions.

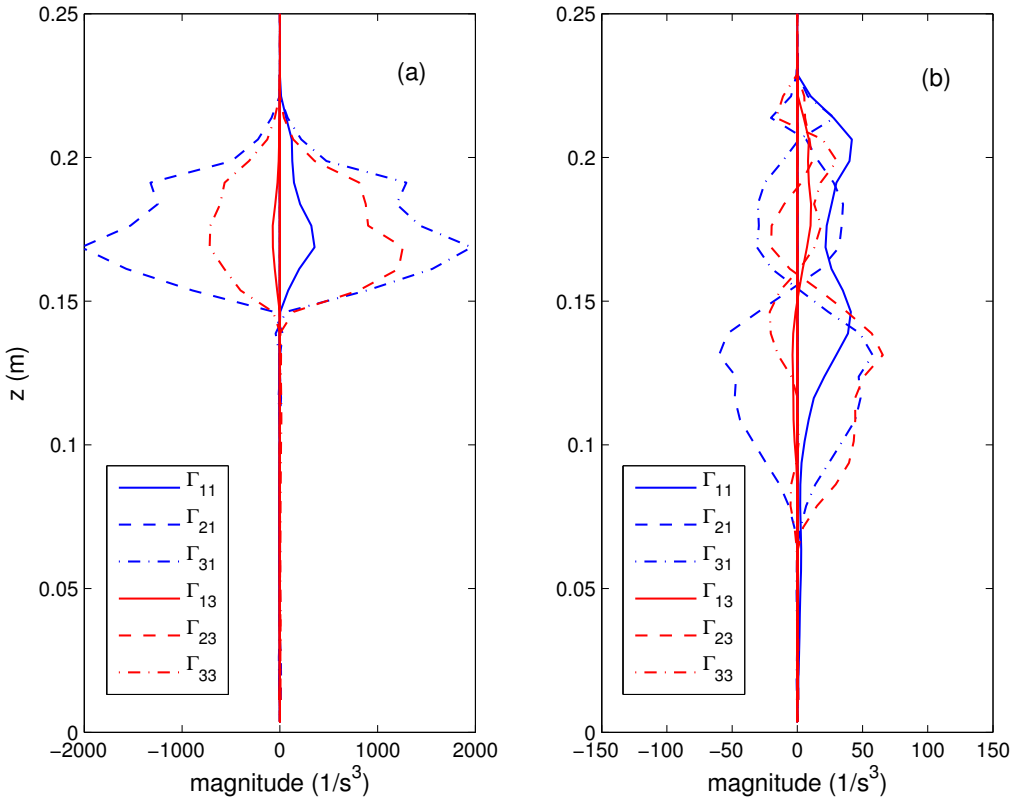

FIGURE 20. Zonal averaged stretching and bending terms in the enstrophy equation at (a) downstream zone BC and (b) upstream zone AB at $t = t_b + 5/8T$, in which $\Gamma_{11} = \omega_x\omega_x\frac{\partial u}{\partial x}$, $\Gamma_{21} = \omega_x\omega_y\frac{\partial u}{\partial y}$, $\Gamma_{31} = \omega_x\omega_z\frac{\partial u}{\partial z}$, $\Gamma_{13} = \omega_z\omega_x\frac{\partial w}{\partial x}$, $\Gamma_{23} = \omega_z\omega_y\frac{\partial w}{\partial y}$ and $\Gamma_{33} = \omega_z\omega_z\frac{\partial w}{\partial z}$.

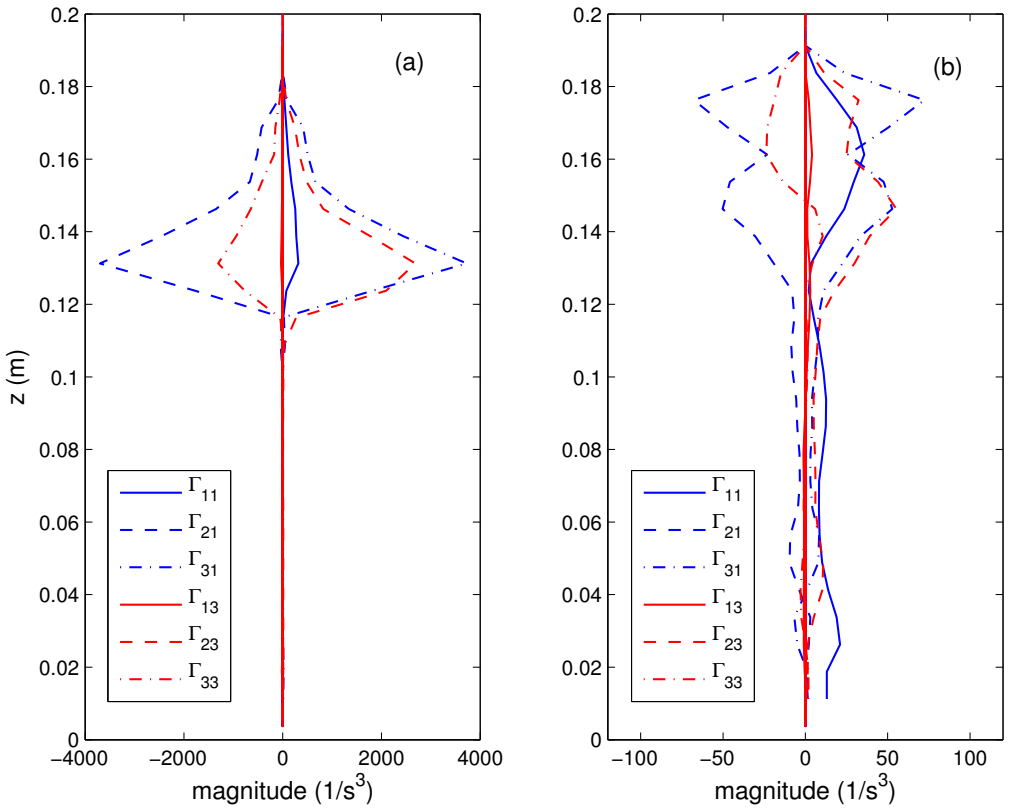

FIGURE 21. Zonal averaged stretching and bending terms in the enstrophy equation at (a) downstream zone BC and (b) upstream zone AB at $t = t_b + 7/8T$, in which $\Gamma_{11} = \omega_x\omega_x\frac{\partial u}{\partial x}$, $\Gamma_{21} = \omega_x\omega_y\frac{\partial u}{\partial y}$, $\Gamma_{31} = \omega_x\omega_z\frac{\partial u}{\partial z}$, $\Gamma_{13} = \omega_z\omega_x\frac{\partial w}{\partial x}$, $\Gamma_{23} = \omega_z\omega_y\frac{\partial w}{\partial y}$ and $\Gamma_{33} = \omega_z\omega_z\frac{\partial w}{\partial z}$.

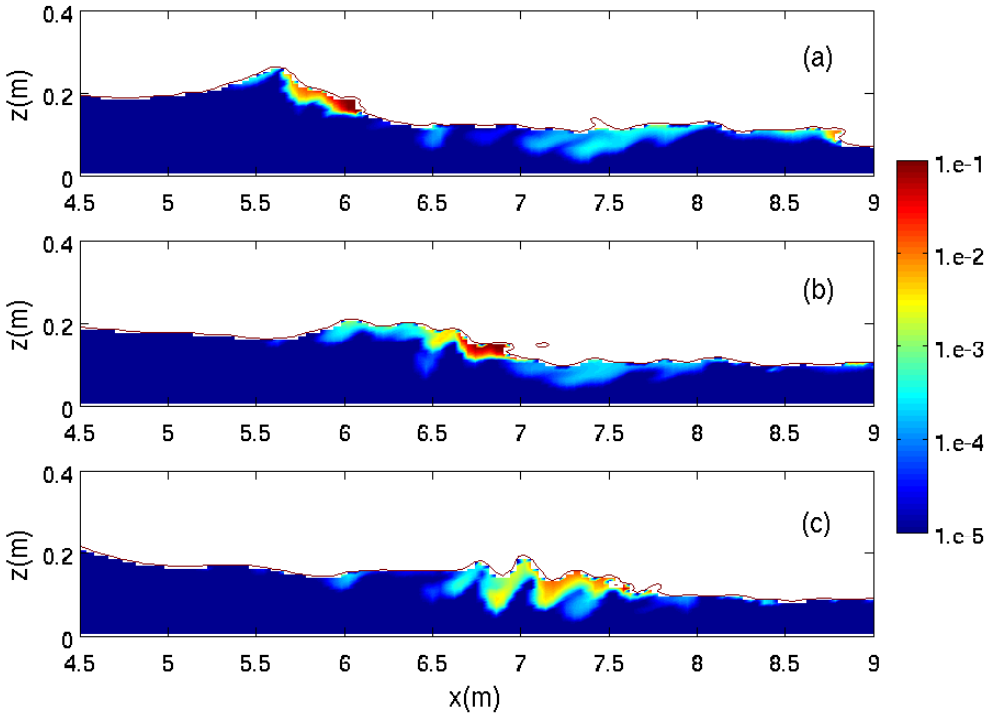

FIGURE 22. Void fraction distributions from a 2D simulation at (a) $t = t_b + 3/8T$; (b) $t = t_b + 5/8T$ and (c) $t = t_b + 7/8T$.

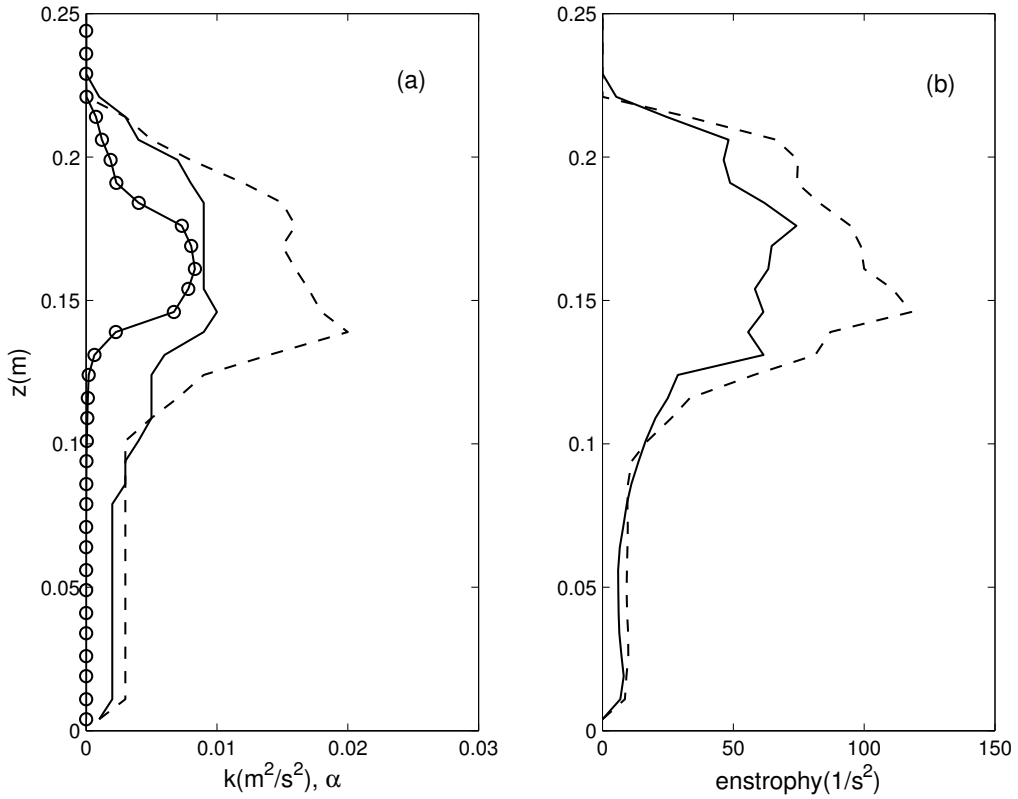

FIGURE 23. Zonal averaged turbulent kinetic energy and enstrophy with (solid lines) and without (dashed lines) bubble effects at $t = t_b + 5/8T$. The solid-circle line shows the zonal averaged void fraction distribution. The zone used to do averaging covers the whole wave length.

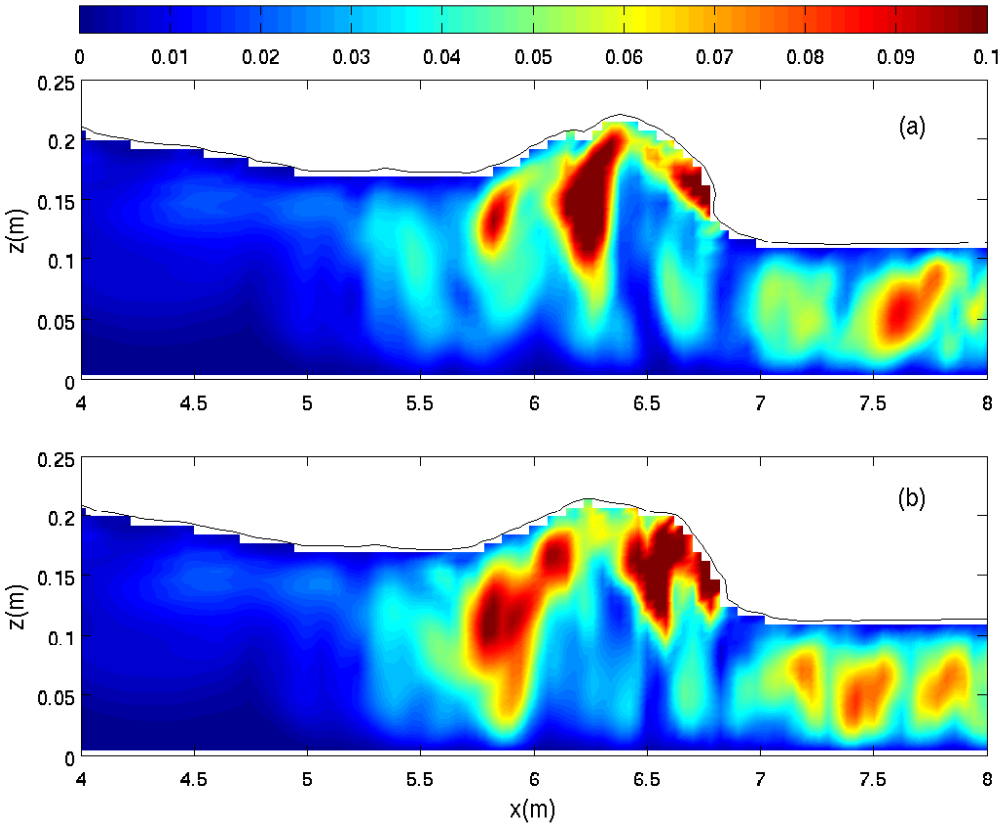

FIGURE 24. The spanwise averaged vertical turbulent velocity $\sqrt{w'^2}$ at $t = t_b + 5/8T$ with (a) and without (b) bubble effects.

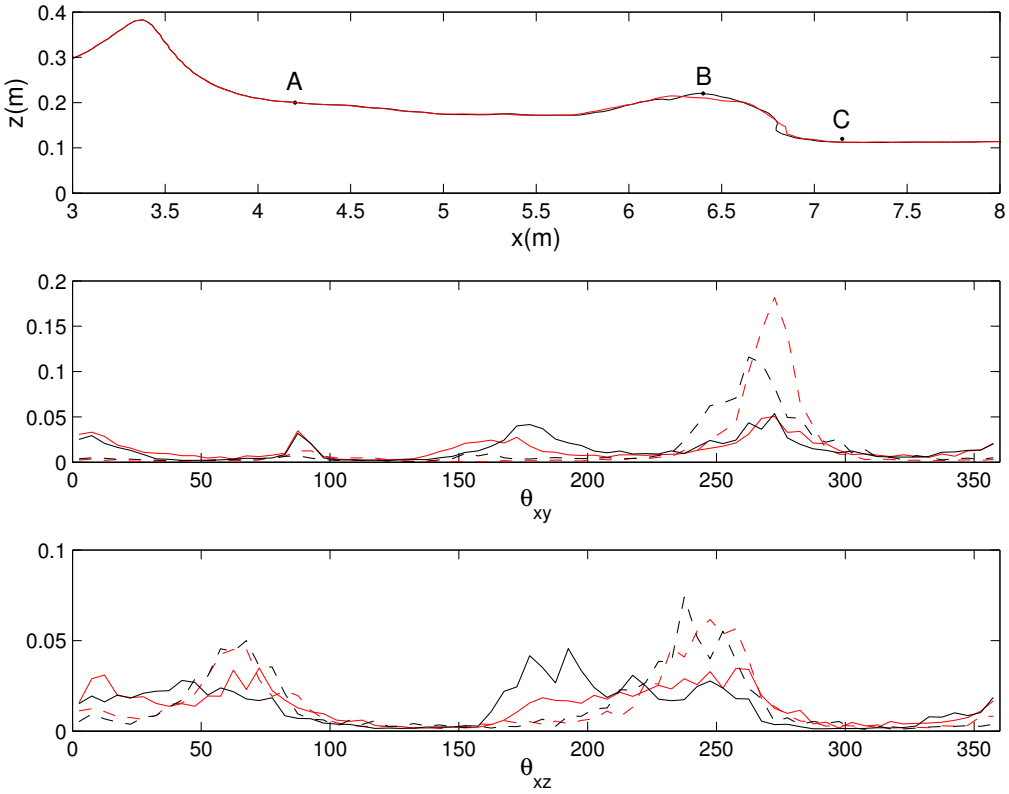

FIGURE 25. Bubble effects on the statistics of vortex structures at $t = t_b + 5/8T$. Dark solid line: upstream without bubbles; Dark dashed line: downstream without bubbles; Red solid line: upstream with bubbles; Red dashed line: downstream with bubbles.